High-Resolution Simulations of the 2010 Pakistan Flood Event: Sensitivity to Parameterizations and Initialization Time

Original
High-Resolution Simulations of the 2010 Pakistan Flood Event:
Sensitivity to Parameterizations and Initialization Time / Viterbo, F., von Hardenberg, J., Provenzale, A., Molini, L., Parodi, A., Ousmane O., S.y., Tanelli, S.. - In: JOURNAL OF HYDROMETEOROLOGY. - ISSN 1525-755X. - 17:4(2016), pp. 1147-1167. [10.1175/JHM-D-15-0098.1]

Publisher:
AMER METEOROLOGICAL SOC

Published
DOI:10.1175/JHM-D-15-0098.1

High-Resolution Simulations of the 2010 Pakistan Flood Event: Sensitivity to Parameterizations and Initialization Time

FRANCESCA VITERBO

Institute of Atmospheric Sciences and Climate, National Research Council, Turin, and University of Genova, Genoa, Italy

JOST VON HARDENBERG

Institute of Atmospheric Sciences and Climate, National Research Council, Turin, Italy

ANTONELLO PROVENZALE

Institute of Geosciences and Earth Resources, National Research Council, Pisa, Italy

LUCA MOLINI AND ANTONIO PARODI

CIMA Foundation, Savona, Italy

OUSMANE O. SY AND SIMONE TANELLI

Jet Propulsion Laboratory, California Institute of Technology, Pasadena, California

(Manuscript received 16 June 2015, in final form 18 January 2016)

ABSTRACT

Estimating the risk of flood-generating precipitation events in high-mountain regions with complex orography is a difficult but crucial task. Quantitative precipitation forecasts (QPFs) at fine resolution are an essential ingredient to address this issue. Along these lines, the ability of the Weather Research and Forecasting (WRF) Model, operated at 3.5-km grid spacing, to reproduce the extreme meteorological event that led to the 2010 Pakistan flood and produced heavy monsoonal rain in the Indus basin is explored. The model results are compared with Tropical Rainfall Measuring Mission (TRMM) rainfall estimates, the available ground measurements, and radar observations from the *CloudSat* mission. In particular, the sensitivity of the WRF simulations to the use of different convective closures (explicit and Kain–Fritsch) and microphysical parameterizations (WRF single-moment 6-class microphysics scheme and Thompson) is analyzed. The impact of using different initial conditions, associated with a different initialization day, is also examined. The use of the new-generation Distributed Simulation and Stimulation System NASA Earth Observing System Simulators Suite radar simulator allows a more accurate and extensive representation of the mesoscale processes and of the interaction with the complex orography. The results reported here indicate that the quality of the large-scale initial conditions is a prominent factor affecting the possibility of retrieving a realistic representation of this event when using a nonhydrostatic regional model.

1. Introduction

In 2010, Pakistan experienced a major flood event that started in late July and was triggered by persistent heavy monsoonal rains. Nearly one-fifth of the entire territory of Pakistan was submerged during the floods (Houze et al. 2011), and at the 19 August 2010 UN General Assembly, Secretary-General Ban Ki-moon defined the consequences of this event as a global disaster.

The meteorological conditions that led to the 2010 Pakistan flooding were rather special when compared to the standard summer monsoon season (Webster et al. 2011; Houze et al. 2011; Rasmussen et al. 2015). The predictability of such unusual conditions and of this specific event from planetary and large-scale synoptic

---

Corresponding author address: Francesca Viterbo, Institute of Atmospheric Sciences and Climate, National Research Council, Corso Fiume 4, 10133 Turin, Italy.
E-mail: f.viterbo@isac.cnr.it

DOI: 10.1175/JHM-D-15-0098.1

conditions down to the mesoscale storm structures was explored in Rasmussen et al. (2015), analyzing European Centre for Medium-Range Weather Forecasts (ECMWF) ensemble forecasts: the synoptic pattern largely responsible for the conditions that generated the Pakistan flooding event in 2010 could be predicted over a week in advance with significant confidence [as stated also by the study of Webster et al. (2011)]. However, the complex topography of the region also played a significant role in the mesoscale development of the event and in determining the detailed rainfall distribution over the area (Rasmussen et al. 2015). In particular, the presence of the Hindu Kush–Karakoram–Himalaya (HKKH) range is a potential source of severe uncertainty in numerical simulations and forecasts and cannot be properly captured by coarse-grid-spaced general circulation models (GCMs). ECMWF and Global Forecast System (GFS) products are available at grid spacing between 0.5° and 0.75°, and even if the precipitation forecast was predictable with reasonably good skills, convective features of the event and orographic characteristics act on scales finer than the GCM pixel resolution and could not be appreciated. Different available forecast and remote observation products reproduced daily rainfall estimates of the July 2010 flood, strongly influenced by their resolutions in capturing the magnitude and the features of precipitation.

In such a complex topography, areas separated by a relatively limited horizontal distance may exhibit a large variability of the spatial–temporal rainfall properties, which are affected by steepness, altitude, temperature, and small-scale orographic characteristics (Anders et al. 2006). A higher level of detail is then needed to describe the small-scale features of the event. For this purpose, the Weather Research and Forecasting (WRF) Model, operated at 3.5 km, is used to investigate the ability to represent the small-scale atmospheric processes responsible for the event, and we have focused part of the analysis on the vertical structure. The nonhydrostatic characteristic of the WRF Model permits calculating the vertical accelerations and motion explicitly, without determining them diagnostically from the horizontal divergence (as hydrostatic GCMs do). The use of a nonhydrostatic approach permits us to obtain simulations at higher spatial and temporal resolutions, and it is generally applied when the scale of the phenomena is similar to the height scale, such as mesoscale and convective storms. In addition, higher resolution also results in more finely resolved orographic features of the simulations. In the evolution of the dynamics of the model, differences in terms of circulation, due to more finely or coarsely resolved orography, play an important role: in particular, the presence of valleys and ridges results in different local circulations (see also Yu and Teixeira 2014; Flesch and Reuter 2012; Jung et al. 2012). Even if the predictability of the event from the large scales was demonstrated by Webster et al. (2011), small differences in the local circulation and interaction with the orographic features of the region could produce different results at the mesoscale. Subgrid-scale parameterizations and initial conditions can play different roles in determining the predictability of the event at different scales.

In a recent paper, Ushiyama et al. (2014) discussed forecasts of the 2010 Pakistan flood event provided by the WRF Model at 5-km resolution [Kain–Fritsch (KF) cumulus parameterization and WRF single-moment 3-class (WSM3) microphysics] forced by the National Centers for Environmental Prediction (NCEP) GFS. They show that the dynamically downscaled forecasts predicted reliable amounts of rainfall in the Kabul River basin 1 day ahead of the rainfall onset and predicted a high probability of heavy rainfall 3 days ahead. In this work we adopt a finer and cloud-permitting grid spacing (3.5 vs 5 km) in the innermost WRF domain, which is 7 times wider (3807 km × 2643 km vs 1245 km × 1125 km) than the one used by Ushiyama et al. (2014). This allows us to better capture, also at cloud-permitting resolution, the interaction between the mesoscale circulation and the synoptic situation, over the considered complex topography area, whose role has been crucial for the spatiotemporal evolution of this case study. To do that, a finer vertical grid spacing (42 vs 28 vertical levels) is needed to capture more accurately the topographic role on the spatiotemporal evolution of this case study. Two different microphysics schemes (WSM6 and Thompson) instead of only one (WSM3) have been adopted, as well as three different convection parameterization approaches (KF, Betts–Miller–Janjić, and explicit) versus one (KF).

Again, using the WRF Model, Ullah and Shouting (2013) showed that a high midtropospheric potential vorticity anomaly led to the development of a strong mesoscale convective vortex and to large-scale cyclonic circulation over Pakistan during the summer monsoon of 2010. The symmetric instability consequent to the negative moist potential vorticity anomaly significantly enhanced the vertical ascending and precipitation in the convective area (Ullah and Shouting 2013). In such applications, however, the details of the parameterizations and boundary and initial conditions adopted in the mesoscale model play a crucial role, and the sensitivity of the results to these factors needs to be carefully addressed and better understood, especially in the case of such a high-impact weather event (HIWE) over an extremely complex topography area. To address these issues, we analyze the role of different convection and microphysics parameterizations, and we investigate the sensitivity to the choice of the initial conditions of WRF simulations performed at cloud-permitting resolution for the most intense days of the 2010 Pakistan flood (26–31 July 2010).

The outputs of the model in terms of daily rainfall are compared with estimates provided by the TRMM satellite (Kummerow et al. 1998) and by rain gauge stations. We also investigate the vertical structure of the atmosphere by means of *CloudSat* observations, comparing them with the WRF simulations using the Distributed Simulation and Stimulation System (DS3) simulator (Tanelli et al. 2002) included in the NASA Earth Observing System Simulators Suite (NEOS^3; Tanelli et al. 2012). In the analysis presented and discussed here, the test case of the 2010 Pakistan flood can be considered as an HIWE case study where the ability of numerical weather models is seriously challenged.

2. Event overview

In early July 2010, a strong ridge of high pressure began to develop near the Ural Mountains in Russia, creating an ''Omega''-shaped blocking pattern over Europe throughout western Russia that lasted for at least 2 months. This high pressure center created an abnormally active jet stream riding around the perimeter of the blocking into western Pakistan, acting as a carrier of hot and moist air and creating a ''supercharged monsoon'' associated with unstable atmospheric conditions (Hong et al. 2011). The interaction between strong tropical monsoon surges and extratropical disturbances downstream of the blocking became crucial in triggering the flood (Hong et al. 2011). In normal monsoonal events, the low-level moisture flow originates predominantly from the Bay of Bengal, with smaller contributions from the Arabian Sea (Houze et al. 2011). In this case, however, the low-level anomaly in the moisture flux introduced by the indirect contribution of a La Niña phase in South and Southeast Asia had a strong effect in weakening the eastward moisture transport and in helping to enhance the moisture transport and convergence in the northern Arabian Sea and Pakistan (Hong et al. 2011). Figures 1e, 1j, and 1o and Figs. 2e, 2j, and 2o show large-scale fields of geopotential, temperature, and specific humidity of ERA-Interim (Dee et al. 2011) at 500 hPa, in comparison with the results obtained in the WRF runs (discussed more deeply in section 5). This situation represented by the reanalysis resulted in an unusual displacement of the heavy monsoonal stratiform precipitation patterns, which are typical for the wetlands in northeastern India and Bangladesh, toward the arid mountainous region of northern Pakistan. This anomalous flow extended also to lower levels, carrying moisture toward the Himalayan barrier and leading to a favorable environment for the mesoscale rain systems (Hong et al. 2011). The European blocking acted on the persistence of this event. Moist air was blocked inside a mountain region of usually dry air, leading to the anticipation of saturation conditions. This caused a less convective vertical growing of the cells and a more stratiform horizontal extension due to upslope flow with respect to what happens in normal monsoonal events in that mountain region (Houze et al. 2011).

The most consistent heavy rainfall event occurred from 27 to 30 July. Galarneau et al. (2012) give a good description of the development of convection, analyzing *Meteosat-7* and TRMM images. From late 27 July to 0600 UTC 28 July, an intense convective event with evidence of possible widespread stratiform precipitation started to impact southwestern Pakistan (Houze et al. 2011; Galarneau et al. 2012). Then the rainfall moved toward the high-mountain region in northern Pakistan and persisted over the same region for nearly 24 h from 1200 UTC 28 July to 1200 UTC 29 July, with a continuous redevelopment of convection. The extremely moist environment increased precipitation efficiency and mitigated the cold pool development that could propagate the convection away from mountains. Finally, on 30 July, only light rain persisted over the northern Pakistan area and the highest precipitation shifted over west-central India (Galarneau et al. 2012).

In conclusion, the event was characterized by a close interaction between larger and smaller scales and by a strong orographic component (Rasmussen et al. 2015).

3. Experimental setup

a. The WRF Model

The WRF Model, version 3.3.1, is a fully compressible, nonhydrostatic, scalar variable–preserving mesoscale model (Skamarock et al. 2008). The runs analyzed in this study are performed using two domains (Fig. 3): an external domain (d01), extending in the range 2.59°–55.52°N and 50.69°–96.11°W, resolved at 14 km; and an internal domain (d02), extending in the range 10.12°–49.84°N and 57.08°–90.02°W, resolved at 3.5-km grid spacing. The grid spacing adopted for the innermost domain already belongs to the so-called cloud-permitting range and represents a good compromise between computational performances and capability of representing the key details of the complex topography of the HKKH range, so it is important for the case study under examination. This choice is improving what has been done in literature until now: to provide some examples

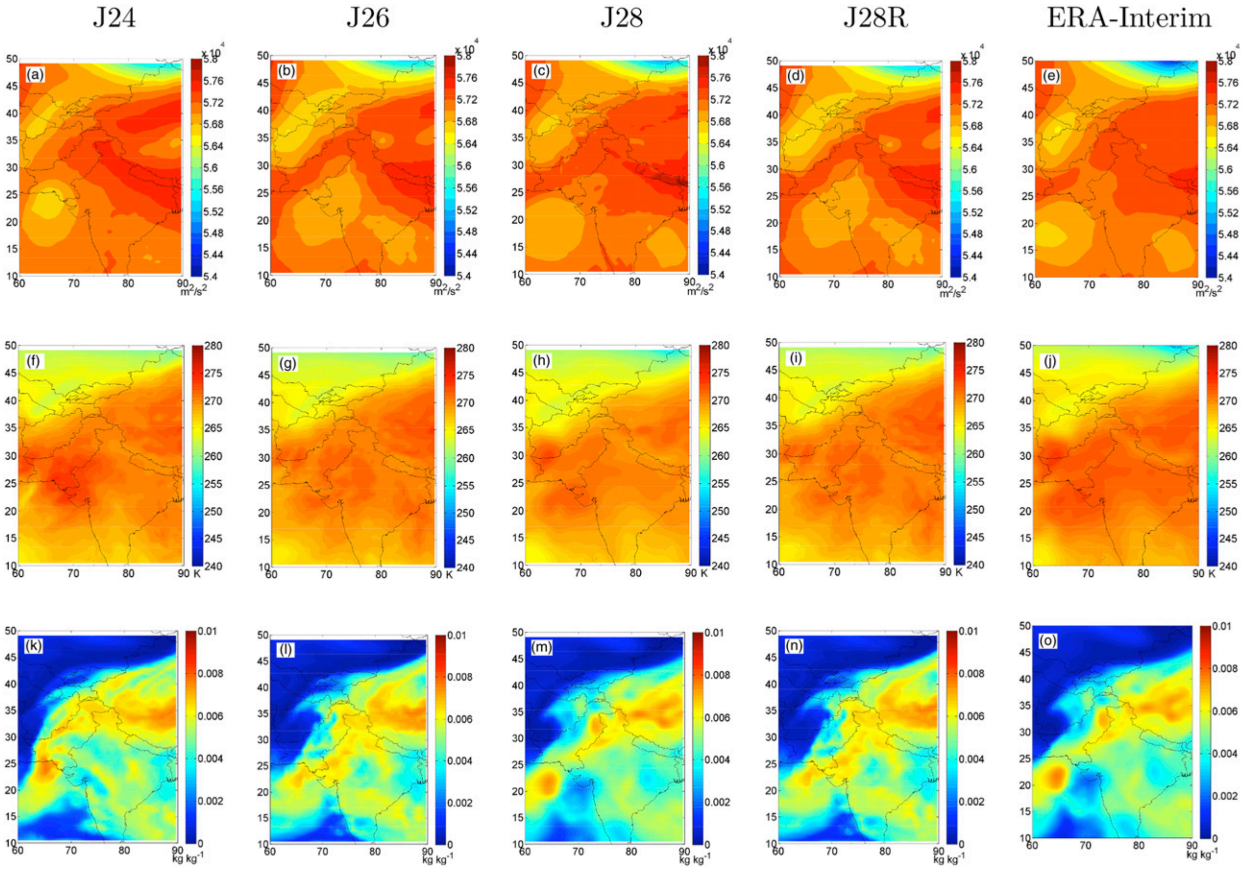

FIG. 1. Large-scale circulation of (a)–(e) geopotential, (f)–(j) temperature, and (k)–(o) specific humidity at 500 hPa at 0000 UTC 28 Jul as simulated (from left to right) by WRF J24, J26, J28, and J28R runs and by ERA-Interim.

of the state of the art, Ushiyama et al. (2014), Ahasan and Khan (2013), and Ullah and Shouting (2013) indeed adopted similar small-domain grid spacing (5, 3, and 3 km, respectively) but on definitely smaller domains (Kabul River basin and a smaller windows in northwestern Pakistan) for the same event. Also, Maussion et al. (2011) performed simulations in the area at 2 km, but in the Tibetan Plateau (with less steep local orography) and again over a less extended domain.

Figure 3 shows the two nested computational domains and the orography of the region, obtained from the 1-min gridded elevations/bathymetry for the world (ETOPO1) dataset (Amante and Eakins 2009). A two-way nesting mode is used to couple the two grids. The vertical dimension is discretized with 42 levels. The turbulent parameterization is the Yonsei University scheme (Hong et al. 2006).

The radiation schemes adopted are the Rapid Radiative Transfer Model (RRTM) scheme for longwave parameterization (Mlawer et al. 1997) and the Goddard scheme for shortwave parameterization (Chou and Suarez 1999).

In areas of complex orography, the high variabilities in elevation, surface slope, and aspect lead to a strong heterogeneity in solar radiation distribution, and by consequence they affect evapotranspiration, moisture and heat fluxes, and soil and air temperature (Chen et al. 2013). In this experiment, the land-use dataset is derived from the U.S. Geological Survey (USGS) 24-category data at 30-arc-s resolution, and the land surface model is the five-layer thermal diffusion scheme from MM5. The experiment has been carried out in hindcast mode, with boundary and initial conditions provided by ERA-Interim fields at the native resolution (0.75°; Dee et al. 2011) representing the latest global reanalysis produced by ECMWF.

b. Microphysical schemes and convective closures

The joint action of the complex topography (due to the presence of the Tibetan Plateau and the HKKH range) and of the climatic features of a monsoon-influenced environment make the choice of the convective and microphysics parameterizations difficult (Sardar et al. 2012).

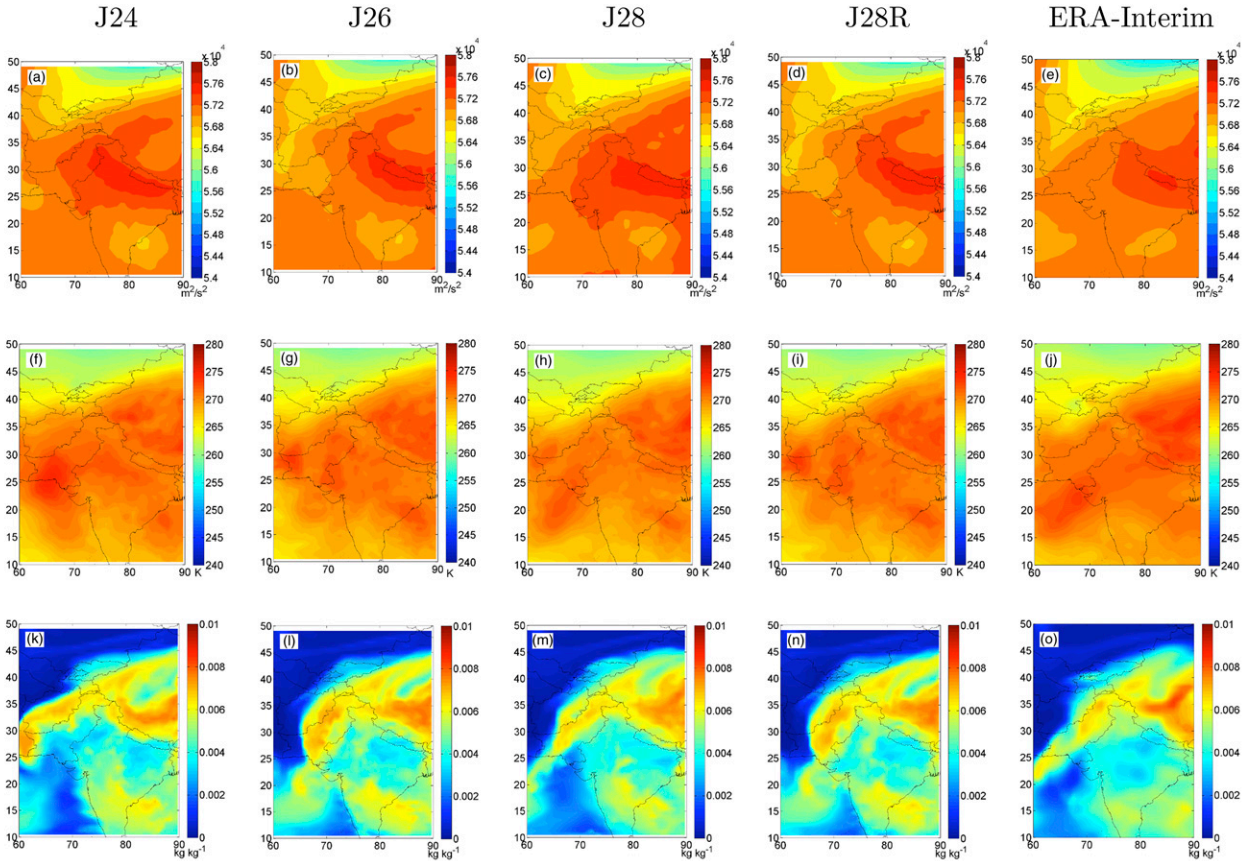

FIG. 2. As in Fig. 1, but for values at 0000 UTC 29 Jul.

For the convective closure schemes, the choice of a 3.5-km horizontal resolution allows us to explicitly resolve (albeit crudely) convective processes (Kain et al. 2006, 2008). A number of studies investigated numerical simulations in the so-called ''gray zone'' of spatial resolution, corresponding roughly to 1–5 km, to understand whether convective parameterization is needed at this resolution (e.g., Gerard 2007; Parodi and Tanelli 2010). Since no definite conclusion on this issue has been reached (e.g., Yu and Lee 2010), in this study we opt for running simulations with either a parameterized (Kain and Fritsch 1990) or explicitly resolved convection scheme in d02, while the outermost domain at 14 km always adopts parameterized convection (Kain and Fritsch 1990). The choice of KF as parameterized run is motivated by the results and recommendations of previous studies in the region (Ahasan and Khan 2013; Sardar et al. 2012).

With regard to microphysics, the leading idea has been to compare the performances of a single-moment scheme versus a double-moment one when modeling a severe rainfall event, over such an extremely complex topography with a cloud-permitting grid spacing. For this reason, WSM6 (Hong and Lim 2006) and the double-moment Thompson scheme are selected.

WSM6 (Hong and Lim 2006) extends the WRF single-moment 5-class microphysics scheme (WSM5). In this scheme, a new method for representing mixed-phase particle fall speeds for snow and graupel has been introduced. The single fall speed assigned to both classes is weighted by their mixing ratios and is applied to both sedimentation and accretion processes (Dudhia et al. 2008).

The Thompson scheme (Thompson et al. 2008) presents a significant number of improvements in the modeling of physical processes if compared to earlier single-moment approaches, and it takes advantage of results provided by more complex spectral/binned schemes that adopt lookup tables. The assumed snow size distribution depends on ice water content and temperature and is represented as a sum of exponential and gamma distributions. Snow assumes a nonspherical shape with a bulk density that varies inversely with the diameter, as found in observations.

It is certainly true that using WSM6 versus the WRF double-moment 6-class microphysics scheme (WDM6)

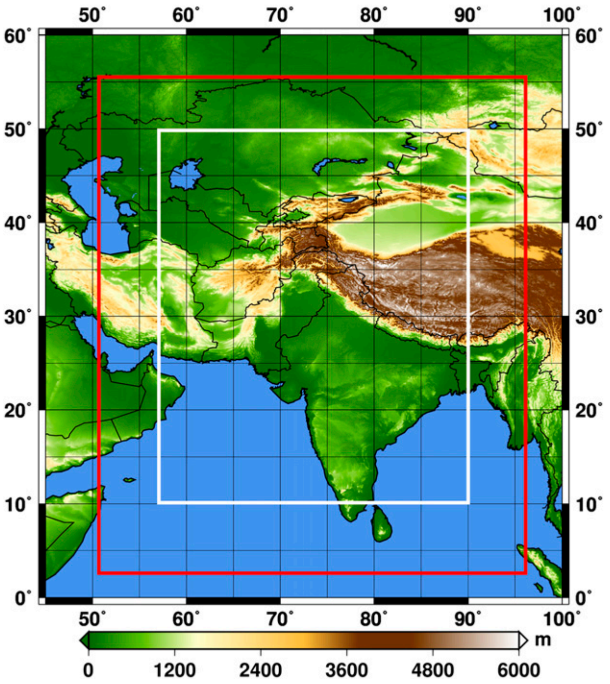

FIG. 3. The two nested domains used for the simulations: external domain (d01; red box) at 14-km resolution and internal domain (d02; white box) at 3.5-km resolution. The color levels report the orography of the region, provided by the ETOPO1 dataset.

(Lim and Hong 2010) would have been a worthy experiment to perform. In this study, we have used WRF, version 3.3.1, and for that version WDM6 was a quite new entry in the microphysics parameterization portfolio, still subjected to testing and bug fixes.

In the external domain (d01; 14 km) we use the KF convective scheme and the same microphysics as in the interior domain.

4. Observational data

The orographic complexity of the region under study and the limited availability of meteorological observations in the area represent two of the main challenges in comparing model results with measured data.

The study of Palazzi et al. (2013) considered and compared different available datasets in the HKKH region and evaluated the capability of these observations in reproducing precipitation characteristics and trends. Andermann et al. (2011) also produced a similar study and gave an overview of gridded available precipitation datasets along the Himalaya front. These studies analyzed the differences between the available products, with similarities and discrepancies. Great caution should be used in comparing pixel values of station observations and remote sensing techniques, especially at high temporal resolution (Andermann et al. 2011), particularly when the resolution of observations is coarser than the spatial variability of rainfall. The study of Bytheway and Kummerow (2013) confirms the previous statement, investigating the uncertainties related to the TRMM 3B42 product at 3-h accumulation and 0.25° resolution. In their global study of TRMM 3B42 uncertainties over land, they conclude that differences in error characteristics are most prevalent at accumulations below 4 mm h^{-1}. At accumulations higher than 10 mm h^{-1}, the uncertainties of the 3-h product converge to values between 75% and 85%. They add that high-uncertainty values are not surprising for fine temporal resolution data. At the daily scale, uncertainty estimates are greater than 100% for low-intensity daily accumulations and decrease to 20% and 40% at higher daily rainfall rates (Bytheway and Kummerow 2013; Huffman 1997; Tian and Peters-Lidard 2010).

Because of the inaccessibility of mountain regions, rain gauge stations are mainly located in valley floors (Fowler and Archer 2006) and, for this reason, regions above 5 km still remain poorly monitored (Palazzi et al. 2013). The available gauge observations in the area are scarce and are largely biased by altitude, mainly because of technical reasons such as the difficulty to measure the snow water equivalent depth and the deflection of precipitation by winds (see, e.g., Winiger et al. 2005; Anders et al. 2006; Barros et al. 2000). On the other hand, remote observations provide spatially complete coverage of precipitation estimates, but local conditions cannot be incorporated in the sensor algorithm, with potentially large errors within each point of the grid space (Andermann et al. 2011). In the work of Andermann et al. (2011), the difficulties of TRMM 3B42, Global Satellite Mapping of Precipitation (GSMaP), and the Climate Prediction Center (CPC) Rainfall Estimator (RFE) to correctly describe the precipitation distribution at elevations higher than 1 km and to capture precipitation in areas of strong orographic effect are stressed. Nevertheless, in the comparison performed by Andermann et al. (2011), the TRMM 3B42 product results have the smallest bulk error in the monsoon period. Another study by Prakash et al. (2016) has compared the real-time TRMM Multisatellite Precipitation Analysis (TMPA) 3B42 and GSMaP estimates against gauge-based measurements by the India Meteorological Department (IMD) at the daily scale, using 2000–10 datasets. They found that these products are able to capture large-scale spatial features of monsoon rainfall, but still have region-specific biases. Generally, they found a TRMM 3B42 overestimation of 21% and a GSMaP underestimation of 22% over all of India, with respect to rain gauge–based datasets. The largest difficulties in rainfall detection have been found in the mountain regions of northeastern India (Jammu and Kashmir region) and in southern peninsular India. Though the study focused on areas in India, the Kashmir and Jammu region neighbors northern Pakistan and is characterized by similar features in terms of monsoon season and high topography.

Taking all this into account, the recommended approach in handling these datasets is a multisensor strategy where a collection of information is carefully evaluated, considering the uncertainties of each single dataset (Palazzi et al. 2013).

Gridded daily rainfall datasets are available from different remote sensing products (e.g., TRMM and GSMaP). Additionally, we have also considered the new PERSIANN–Climate Data Record (CDR) dataset [for more information on this dataset, the reader is referred to Ashouri et al. (2014)]. The precipitation information provided by TRMM, GSMaP, and PERSIANN estimates are coherent among each other and provide an encouraging signal on the quality of the satellite estimates available for this specific event.

The vertical structure of the atmosphere has been measured by the TRMM PR 2A25 overpasses and by the *CloudSat* product, with different times of passing (thus making their comparison and joint analysis not easy or immediate). The TRMM PR 2A25 tracks cut the study area in the south, in a region with only light precipitation; the *CloudSat* track, on the contrary, passes directly over the main system of interest.

We also have considered rain gauge–interpolated maps to provide a source of ground-based measurements, instead of only remotely sensed estimates, in the daily rainfall comparison. In this work we rely mainly on remotely sensed data from TRMM 3B42 and on rain gauge–interpolated maps as quantitative precipitation estimation (QPE) data sources, while *CloudSat* data are used for vertical cross sections. A quick description of the observational datasets used in the paper is given in the following paragraphs.

a. TRMM

The TRMM 3B42 rain products are used as the main QPE source. The purpose of the 3B42 algorithm is to produce TRMM-adjusted merged infrared (IR) precipitation and root-mean-square (RMS) precipitation error estimates. The final gridded estimates have a daily temporal resolution and a 0.25° × 0.25° spatial resolution. Spatial coverage extends from 50°S to 50°N. Although the dataset of the TRMM 3B42 product has a 3-hourly temporal resolution, at the finer temporal scales the incidence of sampling errors can be large. For this reason, in our analysis we consider only daily cumulates. A more accurate description of TRMM is given by Kummerow et al. (1998) and by the official NASA product site (http://disc.sci.gsfc.nasa.gov/TRMM).

To compare WRF and TRMM daily rainfall fields, we first linearly interpolate WRF fields on a grid finer than the target one (1-km grid spacing), and then we aggregate the pixels at the TRMM 0.25° resolution [see also Herrera et al. (2015)]. We did this transformation in order to preserve the area between the two different grids (the WRF curvilinear and the TRMM linear grid). The fields obtained are focused on a geographic window centered on northern Pakistan (23°–40°N in latitude and 66°–78°E in longitude). This study area was characterized by heavy precipitation on 28 and 29 July.

The quantitative comparison between WRF and TRMM is computed using statistical scores derived both from the traditional calculation of percentiles (60th and 95th), root-mean-square error (RMSE), mean bias (MB), and from the method for object-based diagnostic evaluation (MODE). This latter method was developed at the NCAR Research Applications Laboratory and was intended to reproduce a human analyst's evaluation of the forecast performance. In many cases the traditional scores penalize the performance of forecasts without identifying the cause of the poor performance. An object-based analysis becomes particularly relevant when the model is pushed toward high resolution and the localization and episodic characteristics of rain become more important in the verification process. The MODE analysis is performed using a multistep automated process. A convolution filter and a threshold specified by parameters r and t are applied to the raw field to identify the objects. When the objects are identified, some attributes regarding geometrical features of the objects (such as location, size, aspect ratio, and complexity) and precipitation intensity (percentiles, etc.) are measured. These attributes are used to merge objects within the same forecast/observation field, to match forecast and observed objects, and to summarize the performance of the forecast by attribute comparison. Finally, the interest value combines in a total interest function all the attributes computed in the object analysis [as shown in Brown et al. (2007), their Eq. (1)], providing an indicator of the overall performance of matching and merging between different observed and simulated objects. In our experiment we have empirically chosen the convolution disk radius and convolution threshold, so that this choice would recognize precipitation areas similar to what a human would identify. After a set of experiments, we fixed the value of the convolution radius to three grid points and the threshold of the convoluted field to 35 mm day^{-1}. More information about the MODE technique can be found in Davis et al. (2006a,b) and Brown et al. (2007).

b. *Rain gauge stations*

Rain gauge station data have been considered as an additional term of comparison for daily rainfall estimates. A set of 98 stations from the Pakistan Meteorological Department (PMD) monitoring network was collected and linearly interpolated over the focus area. Moreover, we have selected 90 stations that fall inside the geographic window of interest, compared the gauge measures with the nearest-neighbor WRF grid point of the map comparison, and calculated the associated MB and RMSE. The MB and RMSE calculated compared with the rain gauge dataset are obviously not comparable to the same statistics compared with the TRMM dataset. The rain gauge evaluation is computed based on 90 grid points, while the MB and RMSE computed based on TRMM estimates represent a pixel comparison extended to all grid points in the geographic window. Additionally, the two products (rain gauges and satellite products) are accumulated differently. The daily rainfall station data are accumulated from 0300 UTC for the next 24 h, so great caution should be used when comparing them to TRMM data because a 3-h offset has to be considered. Finally, the comparison is strongly influenced by the different nature of ground and satellite instruments and by their different weaknesses and strengths in measuring precipitation in areas with complex orography. Nevertheless, in an area of scarce observations, they provide an additional point for the discussion.

c. CloudSat

The *CloudSat* mission was designed by NASA to measure the vertical structure of clouds from space and to improve global knowledge of cloud abundance, distribution, structure, and radiative properties. The *CloudSat* instrument was launched in April 2006, as a part of the A-Train satellite constellation. The Cloud Profiling Radar (CPR) installed on *CloudSat* is a millimeter-wavelength cloud radar that allows detection of cloud droplets and ice particles forming the cloud masses. The CPR operates at 94 GHz, which represents the best compromise between performance and spacecraft resources, to achieve sufficient cloud detection sensitivity (Tanelli et al. 2008). The data are given to the *CloudSat* geometric profile product (2B-GEOPROF), whose algorithm identifies those levels in the vertical column that contain significant radar echo from hydrometeors and provides an estimate of the radar reflectivity factor for each of these volumes. The CPR provides detailed information on the vertical structure of cloud systems, and it represents a relevant source of information for the evaluation of climate and weather prediction models [for more information, see http://cloudsat.atmos.colostate.edu and Stephens et al. (2008)].

To compare model outputs with satellite estimates, it is necessary to have a simulator converting model quantities into equivalent radar reflectivities. The effects of instrumental sensitivity and attenuation by clouds and precipitation also have to be taken into account (Bony et al. 2009; Haynes et al. 2007). For this reason, NEOS^3 includes the DS3 simulator (Tanelli et al. 2002) that provides forward simulation to evaluate cloud radar and other remote sensing products (Tanelli et al. 2011, 2012). Using this tool, the WRF outputs are compared to *CloudSat* observations considering the two available satellite tracks over northern Pakistan during the days of the event: granule 22608, recorded at around 2100 UTC 28 July, and granule 22615, recorded at around 0800 UTC 29 July. The *CloudSat* observation tracks are provided in Figs. 4 and 5 (blue lines). Since the granule 22615 on 29 July misses the main observed precipitation core (see Fig. 4l or Fig. 5n), the results in section 5 are discussed only for granule 22608.

5. Sensitivity experiments

a. *Sensitivity to the convective and microphysical schemes*

The four different configurations tested in this work are listed in Table 1. Figure 4 shows the precipitation fields produced by the WRF Model for the different parameterization choices, compared with the TRMM estimates and rain gauge observations, in experiments initialized at 0000 UTC 26 July.

When looking at Exp-WSM6 versus KF-WSM6 (Fig. 4a vs Fig. 4b), we see that the KF scheme produces more precipitation and more organized patterns. This is also true for Exp-Thompson versus KF-Thompson (Fig. 4c vs Fig. 4d). Therefore, in general, it appears that the KF scheme tends to overestimate precipitation and to produce more organized rainfall patterns for our case.

The statistical evaluation computed for our experiment using traditional statistics and MODE verification analysis is reported in Table 2. The MODE values considered refer to the higher-intensity object identified by the verification technique that matches with a corresponding object in TRMM. The white contours in Fig. 4 represent the MODE objects. The percentile values indicate that all four configurations tested tend to

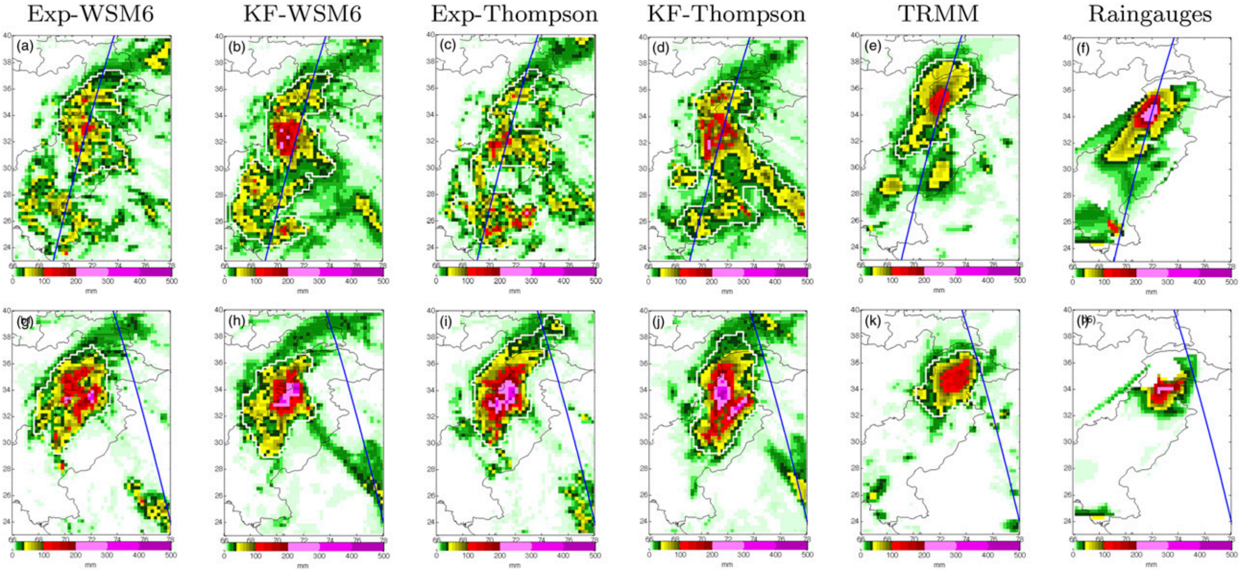

FIG. 4. WRF QPFs and TRMM daily rainfall on (a)–(f) 28 Jul and (g)–(l) 29 Jul 2010 for (from left to right) Exp-WSM6, KF-WSM6, Exp-Thompson, KF-Thompson, TRMM, and rain gauge observations. All fields have been aggregated at 0.25° resolution in the study area. The blue lines represent *CloudSat* tracks and the white contours represent the object identified by MODE analysis.

overestimate the rainfall amount compared to the TRMM estimates, especially for 60th percentile on 28 July and the 95th percentile on 29 July. The percentile values confirm the tendency of the KF simulations to overestimate TRMM estimates. On 28 July, all values of the Exp-WSM6 configuration indicate good accordance with TRMM values. The rainfall intensity given by the percentiles and the localization of the object corresponding to the main precipitation core seem to be best represented by Exp-WSM6. However, on 29 July, the evaluation does not seem univocal: MODE statistical indicators have good agreement with TRMM in terms of total interest and geometric attributes of localization (centroid distance and area ratio) for Thompson microphysics configurations (Exp-Thompson and KF-Thompson), while MB and RMSE have the best results for Exp-WSM6. All values on 28 and (especially) 29 July indicate that the worst results are seemingly obtained using the KF-WSM6 configuration, where the main precipitation core is misplaced and overestimated.

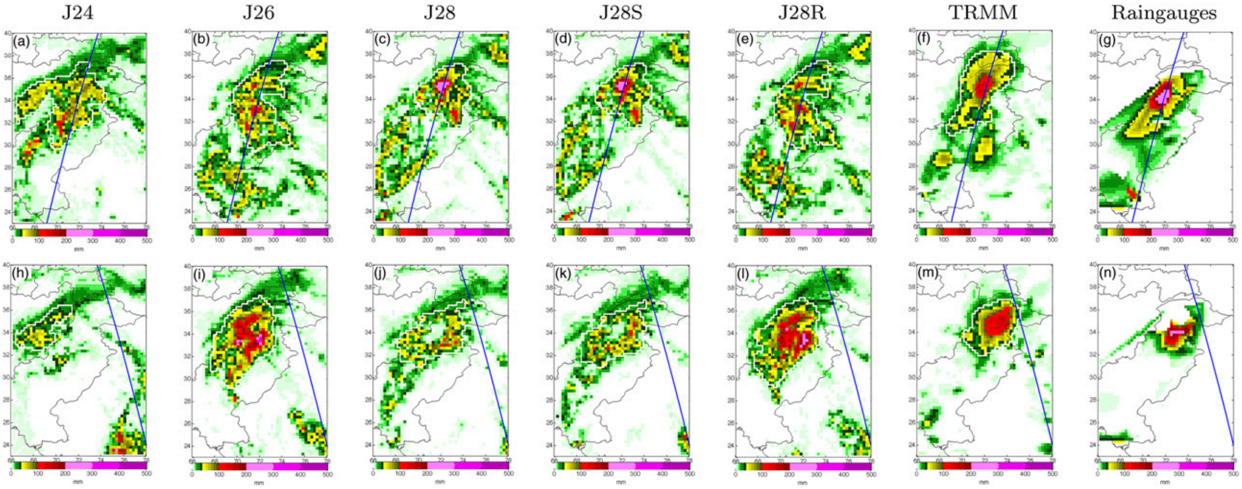

FIG. 5. Accumulation of 24-h rainfall on (a)–(g) 28 Jul and (h)–(n) 29 Jul 2010 for (from left to right) J24, J26, J28, J28S, J28R, TRMM, and rain gauge stations. All fields have been aggregated at 0.25° resolution in the study area. The blue lines represent *CloudSat* tracks and the white contours represent the object identified by MODE analysis.

TABLE 1. Experiment configurations.

Configuration	Convective closure	Microphysics
Exp-WSM6	Explicit	WSM6
KF-WSM6	Kain–Fritsch	WSM6
Exp-Thompson	Explicit	Thompson
KF-Thompson	Kain–Fritsch	Thompson

As a word of caution, however, we note that the differences in score between the different configurations are not very large, and the highly fragmented appearance of the precipitation fields obtained with explicit convection does not entirely match the TRMM data. In addition to that, with equal convective scheme, the Thompson microphysics presents higher 95th percentile values. If we examine the results of the statistics calculated in comparison with the rain gauge datasets (Table 2), the MB estimates on 29 July also confirm the tendency of the Thompson microphysics to produce higher-than-observed rainfall amounts (even if closer to measured values than the other simulations). The WSM6 has been found to produce larger values of evaporation rate over the entire atmospheric column in Bryan and Morrison (2012) and in Morrison et al. (2015) with reference to highly idealized settings with no orography, possibly explaining its reduced precipitation compared to the Thompson scheme. The rain gauge statistics produce less underestimation (meaning higher precipitation values) for KF configurations on 28 July and the best RMSE for Exp-WSM6 on 29 July.

The analysis of cumulative distributions allows us to understand the variability of the precipitation field, and in particular, the tail of the distribution gives important information about the probability of exceedance of the highest values of the precipitation field. Figure 6 confirms that the Exp-WSM6 simulation produces results that are closer to the statistics of the TRMM estimates. While all the other schemes tend to overestimate the probability of extreme precipitation compared to TRMM, on 28 July the Exp-WSM6 configuration generates distributions that are fairly close to the observations. In this case, the main cause of discrepancy with TRMM (reflected in the statistical scores) is due to a misplacement of the precipitation structures, while intensity and frequency are properly reproduced. On 29 July, all schemes tend to significantly overestimate the observed precipitation. Figures 4f and 4l provide another term of comparison with rain gauge ground measurements. Even if, as discussed above, rain gauge stations present several limitations, the QPE provided by rain gauges is higher than TRMM estimates, providing support for the hypothesis of TRMM underestimation instead of a WRF Model overestimation. Again, the Exp-WSM6 configuration is the closest to rain gauge observations.

TABLE 2. Statistical score analysis for the different configurations for 28 and 29 Jul. Shown are the values of MODE verification analysis of centroid distance, area ratio, and interest; the MODE evaluation refers to the highest-intensity object identified in each run that matches with the corresponding TRMM object. The matched objects are shown in Fig. 4. The 60th and 95th percentiles and the MBs and RMSEs are also given, using TRMM as the reference dataset, as well as the MB and RMSE calculated between rain gauge station measures and associated nearest-neighbor WRF grid points.

	Exp-WSM6	KF-WSM6	Exp-Thompson	KF-Thompson	TRMM
28 Jul					
Centroid distance	601	1860	1934	1884	—
Area ratio	0.919	0.452	0.571	0.422	—
Interest	0.961	0.858	0.851	0.842	—
60th percentile	12.19	15.90	12.95	15.15	4.83
95th percentile	53.30	67.74	58.99	71.88	52.08
MB	3.73	8.43	5.28	8.03	—
RMSE	21.46	26.92	27.31	26.66	—
$\mathrm{MB}_{\text{rain gauges}}$	−20.34	−11.56	−14.60	−10.83	—
$\mathrm{RMSE}_{\text{rain gauges}}$	65.49	65.23	68.81	59.14	—
29 Jul					
Centroid distance	967	1208	472	551	—
Area ratio	0.567	0.599	0.544	0.529	—
Interest	0.914	0.899	0.946	0.940	—
60th percentile	3.63	6.55	3.62	5.87	1.04
95th percentile	69.99	62.38	83.57	94.04	44.70
MB	6.05	7.27	8.79	10.62	—
RMSE	30.42	38.12	40.94	40.60	—
$\mathrm{MB}_{\text{rain gauges}}$	−10.41	−10.97	0.44	14.94	—
$\mathrm{RMSE}_{\text{rain gauges}}$	62.54	87.48	96.60	93.46	—

TABLE 3. Summary of all the different runs performed in the second part of the experiment.

Run	Day of initialization	Configuration	Initial conditions	Boundary conditions	High-resolution domain
J26	26 Jul	Exp-WSM6	ERA-Interim	ERA-Interim	10°–50°N, 60°–90°E
J24	24 Jul	Exp-WSM6	ERA-Interim	ERA-Interim	10°–50°N, 60°–90°E
J28	28 Jul	Exp-WSM6	ERA-Interim	ERA-Interim	10°–50°N, 60°–90°E
J28S	28 Jul	Exp-WSM6	ERA-Interim	ERA-Interim	23°–40°N, 66°–78°E
J28R	28 Jul	Exp-WSM6	WRF J26 restarted at 0000 UTC 28 Jul	ERA-Interim	10°–50°N, 60°–90°E

b. *Sensitivity to the initialization date*

Based on the above results, the configuration with explicit convection and WSM6 is selected for further sensitivity analysis. Using this configuration, we perform forecast experiments considering three different initializations at 0000 UTC: 24 July (J24), 26 July (J26), and 28 July (J28) (Table 3). The different initialization experiments have been chosen considering initialization from 1 to 4 days in advance, every 48 h. We choose this range as a good compromise between possible required spinup time of the model and expected model time integration reliability.

The meteorological analysis is performed starting from the large scales (Figs. 1, 2) down to the mesoscale fields for all the different simulations performed, in order to understand the interscale interplay of the phenomena. At larger scales, variables such as geopotential, temperature, and water vapor mixing ratio are interpolated on the vertical 500-hPa isobar level and compared with ERA-Interim. The synoptic features that led to the severe 2010 events in Pakistan are well reproduced by the model for all its different initializations, if compared with the reanalysis. The geopotential underlines the presence of a strong high pressure block in the northern part of the domain. This blocking high, associated with the presence of smaller-scale troughs in the Arabian Sea and in the south of Afghanistan, led to the formation of a strong wind blowing from the Arabian Sea to the northern part of Pakistan. From the examination of water vapor fields, there is a moisture transport associated with the southwesterly winds that brought a high water vapor quantity up to northern Pakistan. Another source of vapor is given by the moisture flux approaching from the Bay of Bengal. The moisture flux convergence supports the accumulation of moisture during the 2 days on which the maximum precipitation occurs (28 and 29 July). The different model runs exhibit similar large-scale circulation, with small differences between the different simulations. Differences start to emerge when we look at the smaller scales, in which the role of orography (valley and ridges) starts to emerge because of the interaction with the small-scale circulation. In this case, small differences in moisture transport or in wind circulation reflect deeply the different distribution of the resulting precipitation fields.

Figure 5 shows the daily precipitation maps for the crucial days of the event (28 and 29 July), also reporting TRMM observations and interpolated observations from the available rain gauge stations. The J24 run simulates rather well the actual rainfall amounts until 27 July, and then downgrades as the event develops further. The J26 run offers a good performance even though the simulation is not able to correctly reproduce

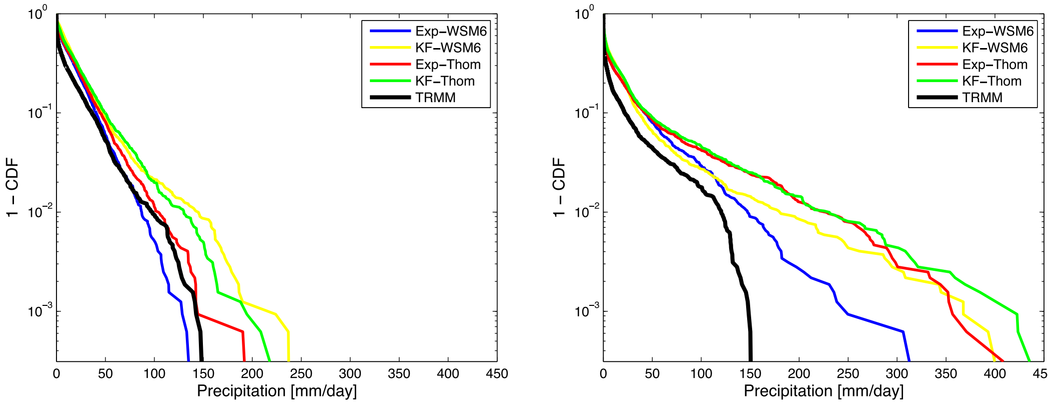

FIG. 6. Comparison between probabilities of exceedance (1 − CDF) for daily rainfall from WRF simulations and TRMM estimates for (left) 28 and (right) 29 Jul. Spatial resolution is 0.25° and the results refer to the whole study area.

the patterns of the first days (26 and 27 July; not shown). For 29 July, the J26 run (Fig. 5i) captures the main rainfall core well, even if it is more widespread and displaced slightly eastward with respect to the observations. The J28 run reproduces well the precipitation pattern on 28 July. On the following day, the J28 run (Fig. 5j) displays a very poor performance, especially when the rainfall pattern of the maximum core is considered. A strong orographic control on the QPF is evident: precipitation is confined to Pakistan plains by the local mountainous range, and the most important precipitation core is completely missed. Because of the poor results of J28 for 29 July, we conclude from the map comparison that the J26 run provides a better forecast of the event.

The J28 run produces higher QPF during its first 24 h of simulation (28 July), and after that the precipitation rates decrease significantly: a possible explanation for this behavior is the dry-out of the atmospheric column caused by the high precipitation rates on 28 July, together with the lack of time for the moisture from the boundaries to gather in the domain in the following 24 h. To test this latter possibility, we reduce the dimension of the domain: the J28 simulation is run again in the two-way nesting mode, but this time the original high-resolution domain (d02) is downsized to the focus area (23°–40°N, 66°–78°E; J28S run). The results obtained for 29 July with the smaller domain do not display any significant improvement, indicating that there must be other causes for the poor performance of the J28 run. In addition to that, the J28S, if compared with J28, shows no sensible dependence of the WRF Model on small perturbation of initial conditions over the time scale of the experiment.

Figure 7 compares the cumulative distributions of daily precipitation for the different initialization dates and for the two target forecast days. The comparison indicates that the J26 run shows a better agreement with the amplitude statistics of the TRMM data. In particular, on 28 July, all other runs (except J24) tend to overestimate the probability of exceedance of precipitation rates larger than about 100 mm day^{-1}. On 29 July, on the contrary, the runs started on the other initialization dates lead to an underestimation of precipitation over the area, even if they are still closer to the TRMM estimates.

Statistical evaluations for the different simulations are summarized in Table 4. The statistical scores partially confirm the previous analysis. The J24 simulation displays a good performance on 28 July and the worst performance on 29 July. On the second day, the interest value of the MODE analysis is extremely low and the geometrical properties of the forecast-observed objects are highly unrelated. For 28 and 29 July, J28 appears to have a good statistical evaluation, even if in the map comparison the pattern of the main precipitation core is totally missed. On the contrary to what is observed in the map comparison, on 29 July the J28 run results in the best values of interest and good percentile values. On the other hand, on 29 July, the 95th percentile confirms the J28 underestimation, even if it is still the closest to TRMM values. If we consider that TRMM tends to underestimate that area (as stated in the previous sections) and the information of the rain gauges, we are more prone to penalize an underestimation of the model rainfall values. The TRMM tendency to underestimate with respect to rain gauges is evident from the comparison between MB related to TRMM and the one based on rain gauge measurements. Even if great caution should be given in the comparison, rain gauge MBs are negative (meaning an underestimation of the model, with respect to the rain gauges), while the MB of TRMM

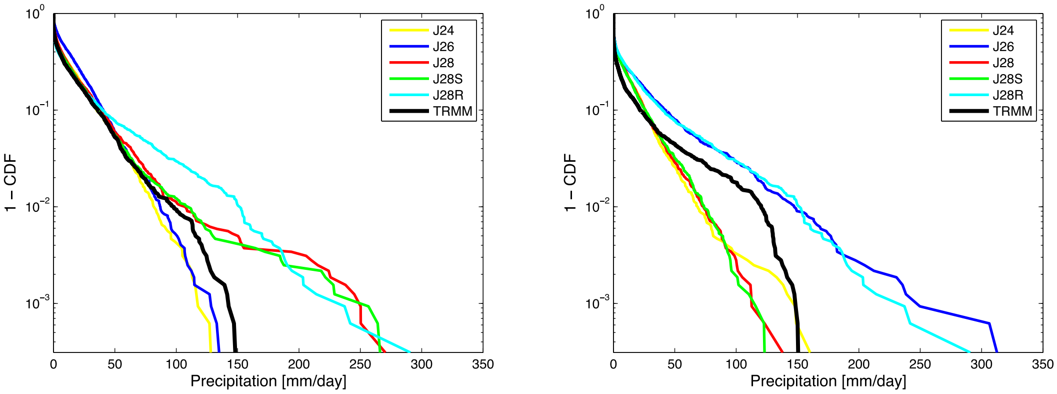

FIG. 7. Comparison between probabilities of exceedance (1 − CDF) obtained from WRF using different initialization days and those derived from TRMM estimates for (left) 28 and (right) 29 Jul. Spatial resolution is 0.25° and the results refer to the whole study area.

TABLE 4. As in Table 2, but for the different initializations on 28 and 29 Jul. The matched objects are shown in Fig. 5.

	J24	J26	J28	TRMM
28 Jul				
Centroid distance	568	601	322	—
Area ratio	0.815	0.919	0.750	—
Interest	0.963	0.961	0.984	—
60th percentile	6.53	12.19	6.69	4.83
95th percentile	53.29	53.30	55.40	52.08
MB	0.77	3.73	1.96	—
RMSE	20.18	21.46	21.80	—
$\mathrm{MB}_{\text{rain gauges}}$	−20.22	−20.34	−9.10	—
$\mathrm{RMSE}_{\text{rain gauges}}$	58.41	65.49	56.31	—
29 Jul				
Centroid distance	1544	967	633	—
Area ratio	0.558	0.567	0.924	—
Interest	0.659	0.914	0.957	—
60th percentile	3.28	3.63	2.80	1.04
95th percentile	36.25	69.99	39.01	44.70
MB	0.31	6.05	0.28	—
RMSE	26.35	30.42	19.24	—
$\mathrm{MB}_{\text{rain gauges}}$	−30.41	−10.41	−18.24	—
$\mathrm{RMSE}_{\text{rain gauges}}$	65.04	62.54	49.83	—

seems to indicate a general overestimation of the model with respect to the satellite estimates. Barring that, the rain gauge statistics are rather in accordance with what is observed in the previous analysis. The MB and RMSE have the best scores for the J28 run on 28 July. On 29 July, J28 still has the best RMSE evaluation, but the best MB is calculated for J26. A lower model underestimation is observed on 29 July for the J26 simulation where the main precipitation pattern is simulated properly.

Nevertheless, the better performance of J26 in the map comparison with respect to J28 on 29 July is rather unexpected, as the J28 run misses the main precipitation pattern.

c. *Sensitivity to initial conditions*

The low QPF performances of the J28 run for 29 July can be related to the role of the specific ERA-Interim initial conditions. In support of these initial conditions, the study of Ahasan and Khan (2013), which was initialized on the same day of J28, but with NCEP–NCAR reanalyses, produced a better rainfall distribution for 29 July (not shown). To test the sensitivity to initialization, we perform a new run, initialized at 0000 UTC 28 July 2010, with a different set of initial conditions. Instead of using the ERA-Interim fields, we run J26 for 48 h until 0000 UTC 28 July. Then all the microphysical variables derived from the WRF dynamics (namely, cloud water, rainwater, snow, cloud ice, and graupel) are set equal to zero: this provides a set of initial conditions comparable with those provided by ERA-Interim [the same required by the WRF Preprocessing System (WPS) for ERA-Interim initialization]. In ERA-Interim we do not have humid variables (microphysical variables), so we have tested the importance of this aspect, initializing the WRF restarted run in the same way. This new set of initial conditions is fed into the model and WRF is run for another 48 h. In this way, we run a novel J28 experiment, initialized with the (partial) output of the J26 run. As shown in Figs. 5 and 7, the results of the J28 restarted (J28R) run outperform the original J28 results: the main precipitation core is modeled well and none of the main precipitation structures is missed. The restarted run produces daily rainfall outputs that are similar to those of J26, providing a better estimate of the main precipitation patterns and positions. Since the only difference between J28 and J28R is the initial conditions, these results suggest that the initial conditions provided by ERA-Interim at 0000 UTC 28 July are mainly responsible for the poor results provided by J28 on 29 July.

To better understand the evolution of the J28 and J28R runs, we compare the surface temperature (Fig. 8) and moisture transport (Fig. 9) at the initialization time (0000 UTC 28 July) and 24 h later (0000 UTC 29 July), at the beginning of the most intense day of the event.

At each horizontal point (pixel), we define the moisture transport as the vertically integrated total moisture transport $\mathbf{F}$ [kg (m s)$^{-1}$] from surface level z_{Surf} to the top of the atmosphere z_{Top} given by the product of the water vapor mixing ratio q (kg kg^{-1}) and the horizontal wind speed $\mathbf{V}$ (m s^{-1}):

$$\mathbf{F} = \int_{z_{\text{Surf}}}^{z_{\text{Top}}} \rho \mathbf{f}\, dz, \quad \text{where} \quad \mathbf{f} = q\mathbf{V},$$

where ρ is the density of air.

At 0000 UTC, the J28R run is identical by construction to the J26 frame. Twenty-four hours later, we find that J28R and J26 present very similar precipitation, as shown in Fig. 5. Surface temperature and moisture transport fields are also very similar, so we choose not to show the J26 run in the comparison of Figs. 8 and 9 to make the comparison clear and straightforward.

The pixel-by-pixel differences for the temperature field at 2 m between the ERA-Interim initialization (J28) and the (partial) WRF initialization (J28R) show strong temperature anomalies (Fig. 8). On 28 July, the J28 field shows a positive bias of more than 3 K in northwestern Pakistan, near the Afghanistan border, and a negative bias eastward (Fig. 8c). The warmer zone of the J28 run can create a stronger instability of the air masses, with a tendency to generate intense precipitation in the next 24 h (on 28 July) and drier and colder atmospheric conditions on 29 July.

The moisture transport reflects the temperature anomalies (Fig. 9). On 28 July, both initializations

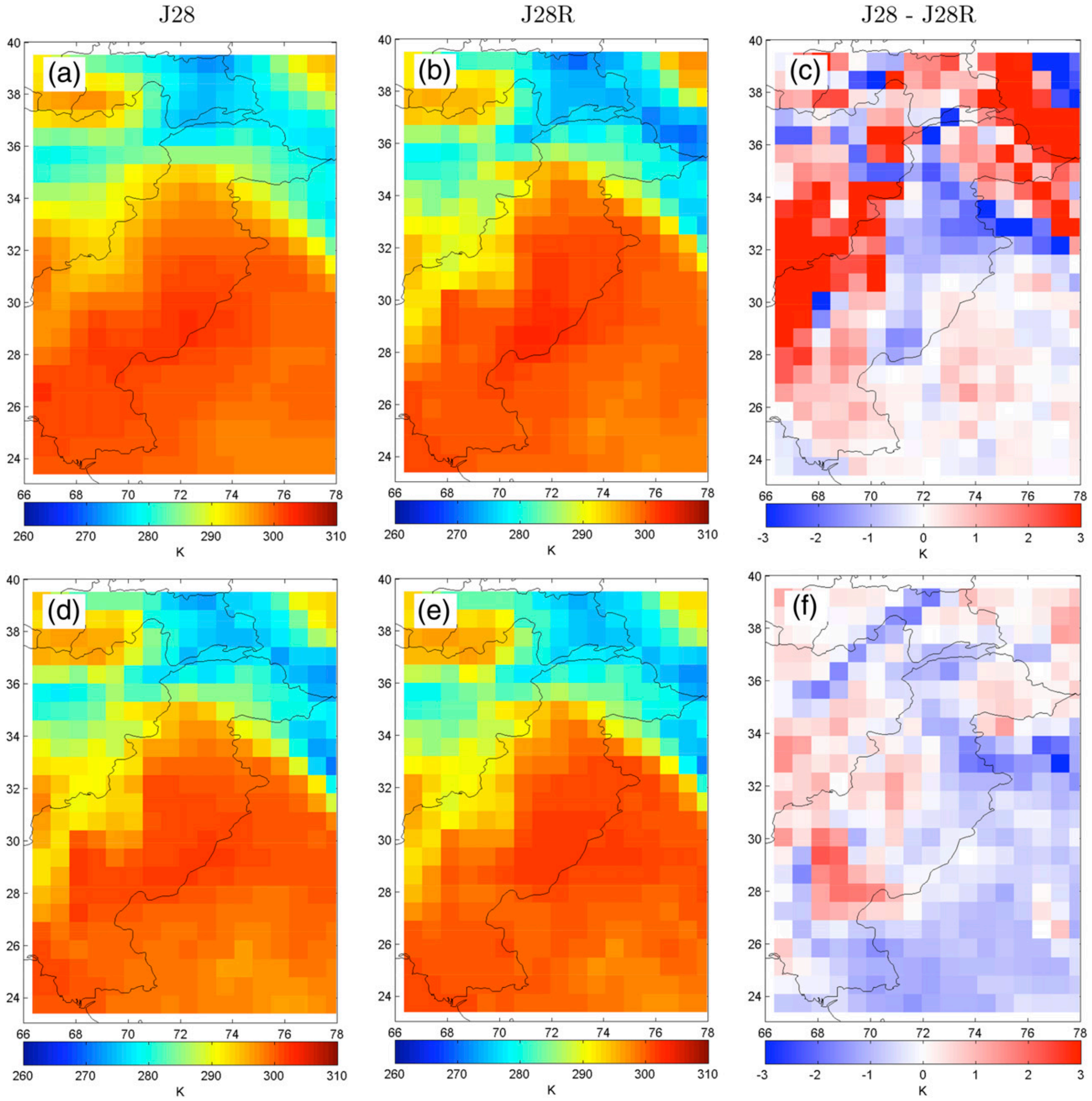
J28

J28R

J28 - J28R

FIG. 8. Surface temperature at (a)–(c) the time of initialization (0000 UTC 28 Jul) and (d)–(f) 0000 UTC 29 Jul for the J28 and J28R runs with (from left to right) temperature field at 2 m in the J28 run, temperature field at 2 m in the J28R run, and pixel-by-pixel difference between these two temperature fields. Temperature fields are plotted at 0.75° horizontal resolution.

generated a moisture transport directed toward the orographic barrier, even if the transport of the J28 run is more concentrated (Figs. 9a,b). The J28R run presents a broader region with a large amount of moisture transport.

The separate contribution of moisture fields and wind fields to total moisture transport has been investigated in terms of horizontal and vertical distributions (not shown). The major contribution of the moisture flow to total moisture transport is always more evident in the southwest part of the domain, for both runs and days of the event. On the contrary, a predominant role of wind is apparent in the northeast part of the study area, over the mountain region. Along the vertical, the highest moisture transport occurs on lower levels, with a major contribution provided by water vapor, instead of wind (which contributes more significantly on higher levels).

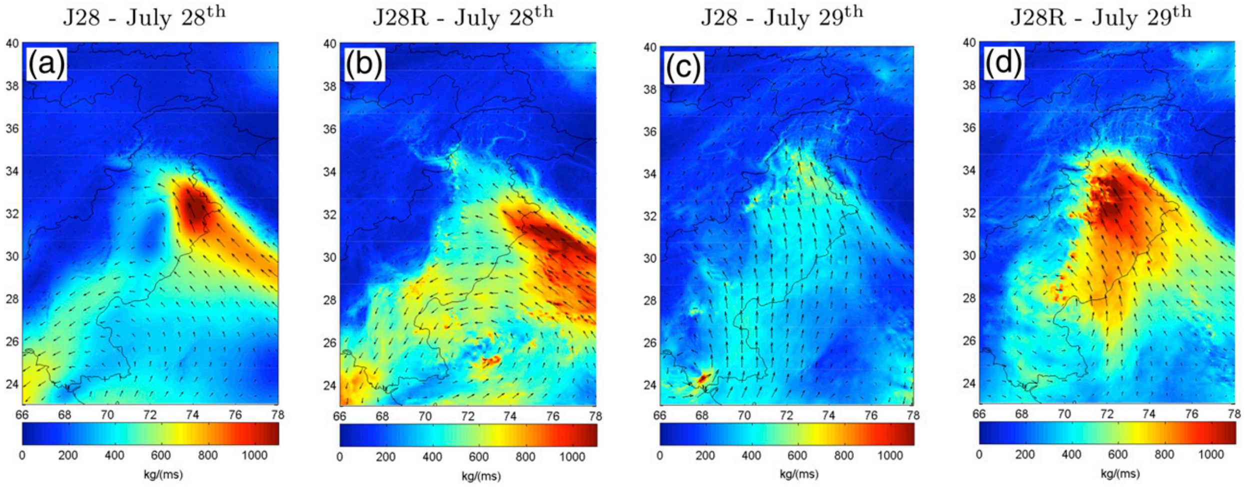

FIG. 9. Moisture transport field for (a) the J28 run at 0000 UTC 28 Jul, (b) the J28R run at 0000 UTC 28 Jul, (c) the J28 run at 0000 UTC 29 Jul, and (d) the J28R run at 0000 UTC 29 Jul. Moisture transport fields are plotted at the resolution of WRF simulations (3.5 km). The colors indicate the intensity and the vectors represent the directions of the moisture transport.

On 28 July, the higher temperatures and the more intense transport are responsible for larger QPF exhibited by the J28 run. The day after (Figs. 9c,d), the J28 run has completely lost the moisture transport contribution, while transport remains high for J28R. In the J28 run there is no moist convergence on 29 July (Fig. 9c), while in J28R the moist air is pushed toward the northern Pakistan orographic barrier producing heavy rain (Fig. 9d). All these factors concurred to create a more intense rainfall spell on 28 July and a drier environment for the following day in the J28 run.

6. Qualitative and quantitative analysis of the vertical structure

Comparison of the surface precipitation patterns against TRMM has allowed us to assess the overall performance of WRF for hydrological purposes. The comparison between the simulated *CloudSat* and *CloudSat* observations provides more insight into the ability of WRF to reproduce vertical profiles of cloud structure.

At 2100 UTC 28 July (granule 22608), *CloudSat* passed directly over the system of interest. A comparison of simulated *CloudSat* using various assumptions and WRF experiments is shown in Fig. 10. As a reference, the *CloudSat* L2B-GEOPROF is provided in Fig. 10a. This graph shows the surface clutter when it is not attenuated by heavy precipitation above it, like around 33°N.

It is evident that the changes in parameterizations and initial conditions result in major differences. These need to be interpreted in light of the temporal and spatial evolution of the system. Therefore, we identify three salient features at the large scale (Fig. 10i) and discuss how each experiment performed in that regard. First, the region of greatest hydrological importance in this portion of this event is the wide and persistent stratiform precipitation area between 33° and 35°N, which was, for the most part, generated by a relatively low convective plume (minimum IR brightness temperatures observed around 230 K) and advected moisture from the southeast (hereinafter STR34N). Second, consider the organized convective towers along the southern part of the line of convergence, characterized by an anvil much less developed than what was observed and top heights of the large hydrometeors (marking convective cores) barely reaching above 10 km, with corresponding IR in the 190–200 K range (hereinafter CONV30N). It is important to note that at the time of the overpass, the line of convective activity curved to the southwest around 29°N along the *CloudSat* ground track (blue line in Fig. 4f and Fig. 5n), and therefore, all convection occurring between 27° and 29°N is not observed by *CloudSat* because it was to the west of the track. Such misplacement is noted here just to address a key feature, namely, the limited representativeness of nadir curtains when interpreting Fig. 10: one should not conclude that a configuration did or did not produce convection according to observations only focusing on these data. The geostationary imagery should always be consulted when interpreting these observations to provide the context that is lacking from the nadir-only profiles. All considerations expressed hereinafter were always developed in this context. The third feature considered is the long outflow associated with STR34N over the

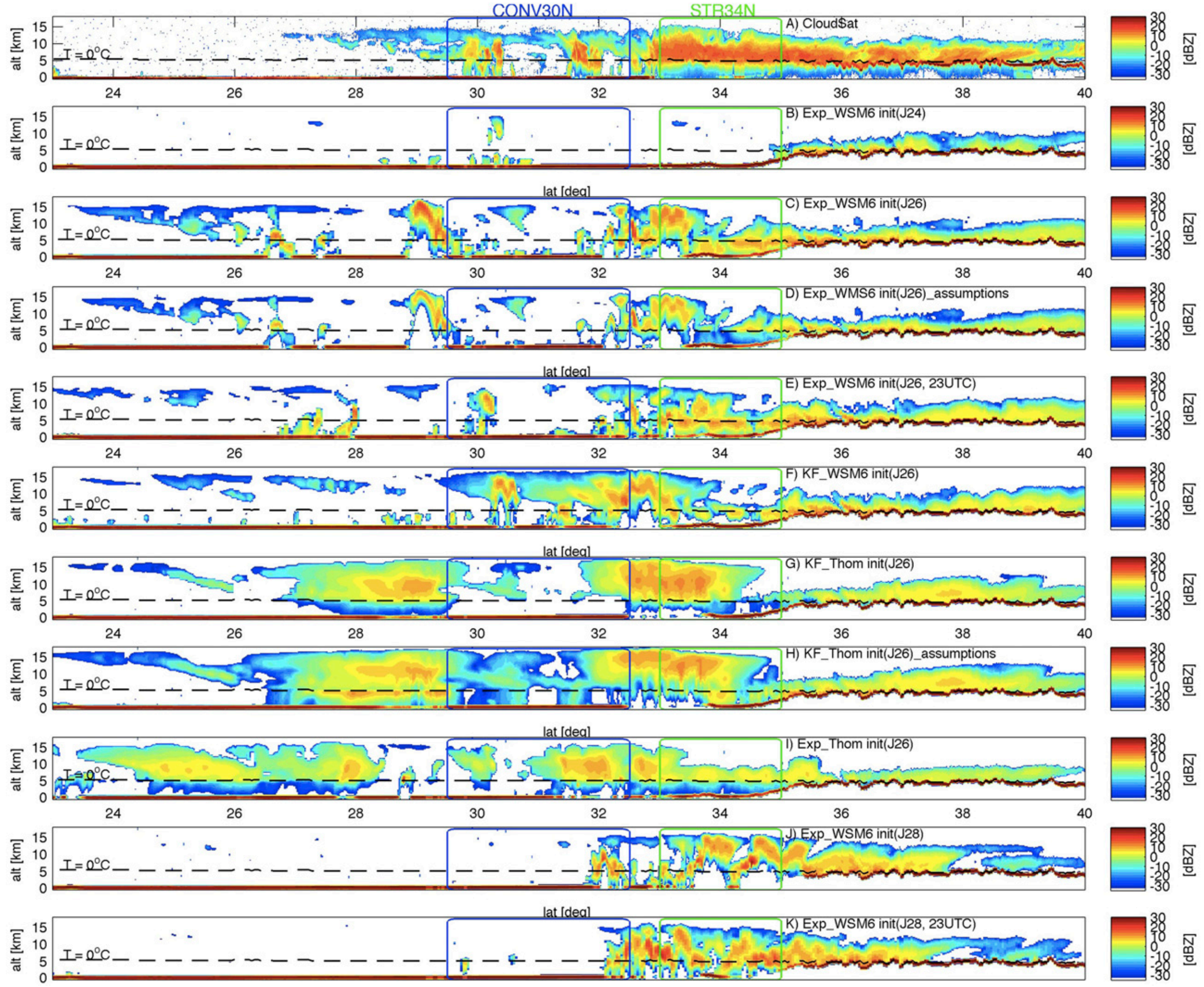

FIG. 10. Vertical structure of the atmosphere at 2100 UTC 28 Jul: (a) *CloudSat* observation (granule 22608) and (b) DS3 *CloudSat* simulations for Exp-WSM6 initialized on J24, (c) Exp-WSM6 initialized on J26, (d) Exp-WSM6 initialized on J26 with different microphysical assumptions, (e) Exp-WSM6 initialized at 2300 UTC on J26, (f) KF-WSM6 initialized on J26, (g) KF-Thompson initialized on J26, (h) KF-Thompson initialized on J26 with different microphysical assumptions, (i) Exp-Thompson initialized on J26, (j) Exp-WSM6 initialized on J28, and (k) Exp-WSM6 initialized at 2300 UTC on J28.

Karakoram range and the Taklimakan desert (latitude from 33° to 35°N) resulting for the most part in snowfall to the surface, but with the zero isotherm in close proximity to the prevailing ground altitude of the desert.

Figure 10b shows that the Exp-WSM6 experiment, initialized on J24, essentially failed to generate precipitation between 33° and 35°N, as also shown in Fig. 5. The CONV30N structure was much suppressed and disorganized; however, a remnant plume did produce snowfall over Karakoram, albeit with cloud-top heights 3 km lower than observed. Figure 10c shows the product of the same configuration but initialized on J26: in this case, all three elements are captured to some extent, but the stratiform region is spatially much less extensive and the convective region extends more to the north and, most importantly, exhibits notably deeper towers than observed (topping at 15–16 km). This comparison confirms that this configuration, while it achieved among the best statistical scores in total precipitation patterns, does not necessarily capture a realistic partitioning in convective versus stratiform precipitation.

To assess the sensitivity of the forward simulations to assumptions independent of the bulk-hydrometeor quantities produced by these single-moment schemes, a series of tests using the same WRF output as input to the *CloudSat* simulation are performed: the assumptions on particle size distribution (PSD) and mass–dimension (m–D) relationship for the hydrometeor species are swapped between those assumed internally in WSM6 and those assumed in the Thompson scheme, plus a third set adopted in airborne precipitation radar microphysical retrievals. In each case the entire set of microphysical assumptions was swapped, and for all of them T-matrix calculations (Mishchenko and Travis 1998) were used to calculate the scattering properties of the hydrometeor species according to the internal assumptions within each module. Oblate spheroids were adopted for raindrops (Beard and Chuang 1987) and snowflakes (Matrosov et al. 2008), and spheres for all other particles.

One example of these tests is shown in Fig. 10d (where both the PSD and *m–D* assumptions of Thompson are applied to the bulk quantities generated by Exp-WSM6 J26). Visual comparison of Figs. 10c and 10d confirms the intuition that at the level of assessment of the general aspect of cloud and precipitation systems, the microphysical assumptions made during the radar simulations are of second-order importance compared to the microphysical assumptions made in the cloud-resolving model simulations. Although the microphysical assumptions at the radar simulation stage change by several decibels the observed reflectivities on various portions of the profile, such change is indeed not sufficient to alter the visual interpretation of the general aspect of the systems other than in a small minority of locations. For example, the only striking difference can be noticed in the rain portion between 33° and 35°N, where the Thompson microphysical assumptions generate reflectivities lower than WSM6 by more than 10 dB. This particular difference is due to the fact that for low water contents WSM6 still assumes raindrops of about 1 mm on average, while the Thompson parameterization results in drop sizes smaller than 0.5 mm (notably, this change was explicitly targeted in that module to better reproduce midlatitude light precipitation and drizzle; Thompson et al. 2008). Therefore, at W band, although the water content is identical (because it comes from the same WRF run), the 0.5-mm particle will be in a Rayleigh scattering regime, unlike the 1 mm, which in turns explains the large differences observed in the radar returns. Overall, an investigation focusing on quantitative retrievals of precipitation must indeed account for them, and the uncertainties within, but when *CloudSat* data are only used to validate the structure of the observed systems assumptions on PSD and scattering models, they become of secondary importance. These tests—performed on each of the WRF experiments—served to eliminate one possible source of ambiguity in the interpretation of the simulated results. Along the same lines, we note that the DS3 simulator has a relatively basic representation of multiple-scattering effects, particularly when compared to the advanced Doppler Multiple-Scattering Simulator (DOMUS; Battaglia and Tanelli 2011), which is included in NEOS[3]. Nonetheless, it was found that the DS3 simulations yielded a more direct interpretation in regard to the nature of the problem. Absence of multiple-scattering effects is, for example, evident in the deep convective storm modeled at 29°N in this simulation where the single-scattering signal is completely attenuated instead of showing the typical stretched echo of multiple scattering all the way to the surface and beyond [see Battaglia et al. (2010) for a comprehensive review on multiple scattering].

Figure 10f shows the product of the KF-WSM6 J26 experiment. Despite identical synoptic conditions and microphysical parameterization, this experiment generates much more developed anvils around CONV30N. However, it fails to capture the stratiform region of greatest interest (STR34N). The low statistical scores quantify the fact that this experiment overestimated precipitation in CONV30N and underestimated it in STR34N. Figures 10g and 10h show the products of KF-Thompson J26 with Thompson and WSM6 assumptions in the radar simulations, respectively. The higher propensity of this microphysical parameterization to produce anvils and resulting stratiform rain is manifested in both cases. The Thompson scheme, unlike a simple single-moment scheme, explicitly predicts the mixing ratio and the number concentration of cloud ice (Thompson et al. 2008). In this scheme, the rain size distribution significantly shifts depending on whether the rain appears to originate from melted ice versus rain produced by collision/coalescence (warm rain). As evident from Figs. 10g–i, the largest reflectivity factors are usually observed above the line of melting level, and the volume above this level is significantly enhanced in the Thompson scheme simulations. Consequently, it generates convection even deeper than WSM6 and produces wider anvils. The latter aspect is more in line with observations, but combined with the former it results in an overestimation with respect to TRMM products (Fig. 6). Comparison to the *CloudSat* reflectivities in the rain portion shows much smaller values in the model than in the observation: this is likely due to the aforementioned assumption of small raindrops in Thompson and the absence of significant multiple-scattering contribution in the simulation. Small drops result in unattenuated reflectivities that are possibly biased low, and if the water contents are overestimated, the specific attenuation can be larger than observations (it is almost independent from drop size). These two factors, combined with the absence of multiple-scattering stretched echo generated in the ice region above, provide a framework to explain this particular difference. Notably, the model runs used to generate these simulated *CloudSat* products apparently extend the region with precipitation more southward than observations. This is because the line of convergence mentioned before did not bend southwest at 29°N as in reality, once again reflecting the great importance of the choice of microphysical parameterizations not only in the resulting storm structures, but also in the large-scale patterns.

Figure 10j shows the product of Exp-WSM6 J28. In this experiment the entire set of features is moved northward and the region of highest accumulation on 28 July is captured better than the other cases, but not because of an improved skill in capturing the nature of the process (which is entirely convective at this time with no significant anvil).

Finally, a perturbation analysis was applied to the simulations to examine the importance of shifting the simulated track relative to the core of the precipitation and the importance of the timing of the WRF run. This is particularly relevant when studying convection, for which location and timing of occurrence are fundamental. To this end, we looked at the satellite simulated overpasses shifted by 0.8° to the east/west with respect to the center of the main precipitation core and using hourly WRF runs in a range of ±3 h around 2100 UTC (time range comparable with the time evolution of these cloud structures). To serve as a reference, the actual *CloudSat* overpass was also overlaid on a map of IR temperature from geostationary satellites. Perturbing the simulated tracks did not reveal any significant improvement and, if anything, led to sometimes missing the main core of the precipitation. For this reason, we focused on the nominal *CloudSat* track. Regarding the timing analysis, we have focused our investigations on J26 and J28 (Exp-WSM6) simulations. For each of these hourly simulations, the simulated radar products were compared to the *CloudSat* measurements in terms of their contour-frequency-by-altitude diagram (CFAD). Namely, we considered a vector consisting of the vertical profiles of the 10%, 50%, and 90% quantiles of the simulated CFADs and compared them to those of the *CloudSat* data. For instance, the correlation coefficient between the CFAD of *CloudSat* measurements and that of the simulated results at 2100 UTC is equal to 85% for J26 (Fig. 10c) and 93% for J28 (Fig. 10j). The strongest correlations to the measurements are observed with the WRF products at 2300 UTC for both J26 and J28, with correlation coefficients of 96% in both cases. The corresponding resulting radar cross sections are depicted in Figs. 10e and 10k for the J26 and J28 runs at 2300 UTC. For the J26 case (Fig. 10e), a comparison with the results at 2100 UTC (Fig. 10c) shows that the clouds and precipitation have moved to the north, as evidenced by the convective cell around 30°N in the CONV30N region. Furthermore, similarly to the *CloudSat* measurements, the top of the cells is lower at 2300 UTC than at 2100 UTC, which explains the slightly larger correlation between CFADs. Nonetheless, there is still a strong resemblance between the features in both instances, for example, in the STR34N region where the precipitation is still disorganized. Similar observations can be made for the Exp-WSM6 case initialized on J28 (Figs. 10j,k), where results at both times capture the persistent precipitation in the mountains (north of 35°N). One can also note the lesser impact of attenuation on the measurements at 2300 UTC in the STR34N region (around 34°N) owing to the lower levels of the clouds at that time.

7. Summary and conclusions

In this paper, we have performed WRF nonhydrostatic simulations at 3.5 km of the HIWE that led to the Pakistan flood in July 2010. We have tested the ability of the modeling system to reproduce the observed precipitation rates and patterns, and we have analyzed the model sensitivity to different microphysics and convection parameterizations and different initializations. Explicit convection and WSM6 turned out to provide a better match in terms of rainfall amount, patterns, and localization when compared to other choices.

Using this configuration, we varied the initialization day to determine the dependence of the model results on the choice of initial and boundary conditions. Even though model outputs are usually more reliable in the first days of the simulation, the J28 run (initialized on 28 July) performed poorly on 29 July, especially when compared to a run initialized on 26 July. This uncommon behavior motivated an additional set of experiments. A new model run (J28R) was initialized on 28 July with the inputs provided by a WRF simulation started on 26 July, with all variables related to clouds and vertical velocities set to zero to be consistent with a standard large-scale initialization. This novel run outperformed the original J28 run initialized with ERA-Interim fields, both in terms of rainfall localization and patterns, as well as daily accumulation, indicating that the initial conditions are a crucial factor in order to obtain a satisfying representation of the event.

The joint use of *CloudSat* observations and simulated cloud radar profiles allowed us to investigate further the skill of each experiment in capturing the most important aspects of the observed vertical structure of this event. In this regard, the Thompson microphysics produces more stratiform precipitation and more organized precipitation patterns than the WSM6, in line with the observations. Both microphysical parameterizations produce convective activity deeper and more intense than observed. Since

Thompson also produces more extensive widespread precipitation from the outflow, it results in an overestimation of the total precipitation. The striking differences in cloud structure resulting from the different microphysical and cumulus parameterizations, even when the same synoptic conditions are adopted, reinforce the assessment that performance of models in reproducing QPE from observations cannot be limited to a few exercises with different models, resolutions, or initial conditions. Notably, the principal differences resulting from the adoption of different parameterizations within a particular model (in this case, WRF) are a consequence of their resulting macroscopic distributions of the bulk quantities of the various hydrometeors and of the different latent heating profiles, and they can radically change the final output of the model given equal initial conditions and resolutions.

Overall, we found that the simulation results are affected more significantly by the choice of the initialization day than by the parameterization schemes adopted. As expected, the largest errors are located near the Himalayas and northern Pakistan, where the steep local orography affected the numerical integration.

The entire study has dealt with the presence of the highest mountain topography in the world, and the experiment of going to 3.5-km resolution with a nonhydrostatic model has represented an instrument to understand the physical processes responsible for the tragic event. In particular, we have found that initial and boundary conditions are prominent factors affecting the results and that small variations in local atmospheric dynamics can produce very different results in complex orography areas. This study has investigated the event at different spatial and temporal scales, starting from large scales down to the mesoscale fields (sections 5b,c) and vertical sections (section 6). The synoptic features of the different initializations in terms of geopotential, temperature, and water vapor mixing ratio are pretty similar for all the runs, and the WRF successfully reproduces the main large-scale features responsible for the event. Moreover, the model, as expected, strongly reflects the large-scale characteristics inherited by the coarsely resolved GCM. The highest differences are evident when the model is challenged to reproduce the smaller-scale features. The different pattern results obtained for the J26 and J28 runs are a manifestation of this: the presence of a valley or of a ridge is capable of strongly influencing the simulation, producing different moisture transport and wind circulation that affect the resulting precipitation fields. As stated in Webster et al. (2011), the predictability of this event was evident from large-scale models, but we agree with Rasmussen et al. (2015), which concludes that a higher degree of detail is needed to understand the anomalous convective features that led to the tragic flooding.

This work focuses on a specific extreme event, namely, the 2010 Pakistan flood, studied using the WRF Model in cloud-permitting mode and operated at 3.5 km in order to gain insight into the predictability of this flood event. While in general it can be difficult to make solid conclusions on the choice of any one or the other microphysics from individual case studies, nonetheless, our results allow us to draw some more general conclusions. In particular, they suggest that a careful choice of parameterization scheme and initialization day must always be adopted, because these factors can significantly affect the simulation. Configurations that exhibit small differences at large scales start to produce very different precipitation amounts, patterns, and circulations, especially over mountain terrain, at small scales. The results presented here indicate that the reliability of the large-scale fields used for initialization and boundary conditions remains an essential ingredient of the simulation and that errors in the large-scale fields can be propagated, or even amplified, in the outputs of high-resolution simulations. For all these reasons, we recommend a dual selection of both initial and boundary conditions and parameterization assumptions to propagate the model through these kinds of events in complex topography areas, rather than an independent analysis of one or another. Interscale phenomena and orography interaction are thus predominant features in studying these particular processes over complex orography areas such as HKKH.

This study intends to contribute to future studies in that area, and it highlights the complexity of studying an HIWE case study in a geographical area in which the ability of numerical weather models is seriously challenged.

Acknowledgments. This work was supported by the PNR 2011–13 Project of National Interest ''NextData'' and by the 2010–11 Project of National Interest ''Innovative methods for water resources management and risk assessment under uncertainty'' of the Italian Ministry for Education, University and Research. The work of Dr. Tanelli and Dr. Sy was carried out at the Jet Propulsion Laboratory, California Institute of Technology, under a contract with the National Aeronautics and Space Administration. This work was carried out in support of the *CloudSat* and GPM missions. The authors are also grateful to the Pakistan Meteorological Department for the provision of the daily rainfall rain gauges data, as well as to the Editor and the four anonymous reviewers for their constructive comments on the early version of the manuscript. The numerical simulations were performed on the SuperMUC Petascale System of the LRZ Supercomputing Centre, Garching, Germany. Project-ID: pr45de.

REFERENCES

Ahasan, M., and A. Khan, 2013: Simulation of a flood producing rainfall event of 29 July 2010 over north-west Pakistan using WRF-ARW Model. *Nat. Hazards*, **69**, 351–363, doi:10.1007/s11069-013-0719-6.

Amante, C., and B. Eakins, 2009: ETOPO1 1 Arc-Minute Global Relief Model: Procedures, data sources and analysis. NOAA Tech. Memo. NESDIS NGDC-24, NOAA NGDC, accessed 17 January 2016, doi:10.7289/V5C8276M.

Andermann, C., S. Bonnet, and R. Gloaguen, 2011: Evaluation of precipitation data sets along the Himalayan front. *Geochem. Geophys. Geosyst.*, **12**, Q07023, doi:10.1029/2011GC003513.

Anders, A. M., G. H. Roe, B. Hallet, D. R. Montgomery, N. J. Finnegan, and J. Putkonen, 2006: Spatial patterns of precipitation and topography in the Himalaya. *Spec. Pap. Geol. Soc. Amer.*, **398**, 39–53, doi:10.1130/2006.2398(03).

Ashouri, H., K.-L. Hsu, S. Sorooshian, D. K. Braithwaite, K. R. Knapp, L. D. Cecil, B. R. Nelson, and O. P. Prat, 2014: PERSIANN-CDR: Daily precipitation climate data record from multisatellite observations for hydrological and climate studies. *Bull. Amer. Meteor. Soc.*, **96**, 69–83, doi:10.1175/BAMS-D-13-00068.1.

Barros, A., M. Joshi, J. Putkonen, and D. Burbank, 2000: A study of the 1999 monsoon rainfall in a mountainous region in central Nepal using TRMM products and rain gauge observations. *Geophys. Res. Lett.*, **27**, 3683–3686, doi:10.1029/2000GL011827.

Battaglia, A., and S. Tanelli, 2011: DOMUS: DOppler MUltiple-Scattering Simulator. *IEEE Trans. Geosci. Remote Sens.*, **49**, 442–450, doi:10.1109/TGRS.2010.2052818.

——, ——, S. Kobayashi, D. Zrnic, R. J. Hogan, and C. Simmer, 2010: Multiple-scattering in radar systems: A review. *J. Quant. Spectrosc. Radiat. Transf.*, **111**, 917–947, doi:10.1016/j.jqsrt.2009.11.024.

Beard, K. V., and C. Chuang, 1987: A new model for the equilibrium shape of raindrops. *J. Atmos. Sci.*, **44**, 1509–1524, doi:10.1175/1520-0469(1987)044<1509:ANMFTE>2.0.CO;2.

Bony, S., M. Webb, B. Stevens, C. Bretherton, S. Klein, and G. Tselioudis, 2009: The Cloud Feedback Model Intercomparison Project: Summary of activities and recommendations for advancing assessments of cloud–climate feedbacks. CFMIP Doc., 19 pp. [Available online at http://cfmip.metoffice.com/CFMIP2_experiments_March20th2009.pdf.]

Brown, B. G., R. Bullock, J. H. Gotway, D. Ahijevych, C. Davis, E. Gilleland, and L. Holland, 2007: Application of the mode object-based verification tool for the evaluation of model precipitation fields. *22nd Conf. on Weather Analysis and Forecasting/18th Conf. on Numerical Weather Prediction*, Park City, UT, Amer. Meteor. Soc., 10A.2. [Available online at https://ams.confex.com/ams/22WAF18NWP/techprogram/paper_124856.htm.]

Bryan, G. H., and H. Morrison, 2012: Sensitivity of a simulated squall line to horizontal resolution and parameterization of microphysics. *Mon. Wea. Rev.*, **140**, 202–225, doi:10.1175/MWR-D-11-00046.1.

Bytheway, J. L., and C. D. Kummerow, 2013: Inferring the uncertainty of satellite precipitation estimates in data-sparse regions over land. *J. Geophys. Res. Atmos.*, **118**, 9524–9533, doi:10.1002/jgrd.50607.

Chen, X., Z. Su, Y. Ma, K. Yang, and B. Wang, 2013: Estimation of surface energy fluxes under complex terrain of Mt. Qomolangma over the Tibetan Plateau. *Hydrol. Earth Syst. Sci.*, **17**, 1607–1618, doi:10.5194/hess-17-1607-2013.

Chou, M.-D., and M. J. Suarez, 1999: A solar radiation parameterization for atmospheric studies. Technical Report Series on Global Modeling and Data Assimilation, Vol. 15, NASA Tech. Memo. TM-1999-104606, 38 pp. [Available online at http://gmao.gsfc.nasa.gov/pubs/docs/Chou136.pdf.]

Davis, C., B. Brown, and R. Bullock, 2006a: Object-based verification of precipitation forecasts. Part I: Methodology and application to mesoscale rain areas. *Mon. Wea. Rev.*, **134**, 1772–1784, doi:10.1175/MWR3145.1.

——, ——, and ——, 2006b: Object-based verification of precipitation forecasts. Part II: Application to convective rain systems. *Mon. Wea. Rev.*, **134**, 1785–1795, doi:10.1175/MWR3146.1.

Dee, D. P., and Coauthors, 2011: The ERA-Interim reanalysis: Configuration and performance of the data assimilation system. *Quart. J. Roy. Meteor. Soc.*, **137**, 553–597, doi:10.1002/qj.828.

Dudhia, J., S.-Y. Hong, and K.-S. Lim, 2008: A new method for representing mixed-phase particle fall speeds in bulk microphysics parameterizations. *J. Meteor. Soc. Japan*, **86A**, 33–44, doi:10.2151/jmsj.86A.33.

Flesch, T. K., and G. W. Reuter, 2012: WRF Model simulation of two Alberta flooding events and the impact of topography. *J. Hydrometeor.*, **13**, 695–708, doi:10.1175/JHM-D-11-035.1.

Fowler, H., and D. Archer, 2006: Conflicting signals of climatic change in the upper Indus basin. *J. Climate*, **19**, 4276–4293, doi:10.1175/JCLI3860.1.

Galarneau, T. J., Jr., T. M. Hamill, R. M. Dole, and J. Perlwitz, 2012: A multiscale analysis of the extreme weather events over western Russia and northern Pakistan during July 2010. *Mon. Wea. Rev.*, **140**, 1639–1664, doi:10.1175/MWR-D-11-00191.1.

Gerard, L., 2007: An integrated package for subgrid convection, clouds and precipitation compatible with meso-gamma scales. *Quart. J. Roy. Meteor. Soc.*, **133**, 711–730, doi:10.1002/qj.58.

Haynes, J., Z. Luo, G. Stephens, R. Marchand, and A. Bodas-Salcedo, 2007: A multipurpose radar simulation package: QuickBeam. *Bull. Amer. Meteor. Soc.*, **88**, 1723–1727, doi:10.1175/BAMS-88-11-1723.

Herrera, S., J. Fernández, and J. Gutiérrez, 2015: Update of the Spain02 gridded observational dataset for EURO-CORDEX evaluation: Assessing the effect of the interpolation methodology. *Int. J. Climatol.*, **36**, 900–908, doi:10.1002/joc.4391.

Hong, C.-C., H.-H. Hsu, N.-H. Lin, and H. Chiu, 2011: Roles of European blocking and tropical–extratropical interaction in the 2010 Pakistan flooding. *Geophys. Res. Lett.*, **38**, L13806, doi:10.1029/2011GL047583.

Hong, S.-Y., and J.-O. J. Lim, 2006: The WRF single-moment 6-class microphysics scheme (WSM6). *J. Korean Meteor. Soc.*, **42**, 129–151.

——, Y. Noh, and J. Dudhia, 2006: A new vertical diffusion package with an explicit treatment of entrainment processes. *Mon. Wea. Rev.*, **134**, 2318–2341, doi:10.1175/MWR3199.1.

Houze, R., Jr., K. Rasmussen, S. Medina, S. Brodzik, and U. Romatschke, 2011: Anomalous atmospheric events leading to the summer 2010 floods in Pakistan. *Bull. Amer. Meteor. Soc.*, **92**, 291–298, doi:10.1175/2010BAMS3173.1.

Huffman, G. J., 1997: Estimates of root-mean-square random error for finite samples of estimated precipitation. *J. Appl. Meteor.*, **36**, 1191–1201, doi:10.1175/1520-0450(1997)036<1191:EORMSR>2.0.CO;2.

Jung, S.-H., E.-S. Im, and S.-O. Han, 2012: The effect of topography and sea surface temperature on heavy snowfall in the Yeongdong region: A case study with high resolution WRF simulation. *Asia-Pac. J. Atmos. Sci.*, **48**, 259–273, doi:10.1007/s13143-012-0026-2.

Kain, J. S., and J. M. Fritsch, 1990: A one-dimensional entraining/detraining plume model and its application in convective parameterization. *J. Atmos. Sci.*, **47**, 2784–2802, doi:10.1175/1520-0469(1990)047<2784:AODEPM>2.0.CO;2.

——, S. J. Weiss, J. J. Levit, M. E. Baldwin, and D. R. Bright, 2006: Examination of convection-allowing configurations of the WRF Model for the prediction of severe convective weather: The SPC/NSSL Spring Program 2004. *Wea. Forecasting*, **21**, 167–181, doi:10.1175/WAF906.1.

——, and Coauthors, 2008: Some practical considerations regarding horizontal resolution in the first generation of operational convection-allowing NWP. *Wea. Forecasting*, **23**, 931–952, doi:10.1175/WAF2007106.1.

Kummerow, C., W. Barnes, T. Kozu, J. Shiue, and J. Simpson, 1998: The Tropical Rainfall Measuring Mission (TRMM) sensor package. *J. Atmos. Oceanic Technol.*, **15**, 809–817, doi:10.1175/1520-0426(1998)015<0809:TTRMMT>2.0.CO;2.

Lim, K.-S. S., and S.-Y. Hong, 2010: Development of an effective double-moment cloud microphysics scheme with prognostic cloud condensation nuclei (CCN) for weather and climate models. *Mon. Wea. Rev.*, **138**, 1587–1612, doi:10.1175/2009MWR2968.1.

Matrosov, S. Y., M. D. Shupe, and I. V. Djalalova, 2008: Snowfall retrievals using millimeter-wavelength cloud radars. *J. Appl. Meteor. Climatol.*, **47**, 769–777, doi:10.1175/2007JAMC1768.1.

Maussion, F., D. Scherer, R. Finkelnburg, J. Richters, W. Yang, and T. Yao, 2011: WRF simulation of a precipitation event over the Tibetan Plateau, China—An assessment using remote sensing and ground observations. *Hydrol. Earth Syst. Sci.*, **15**, 1795–1817, doi:10.5194/hess-15-1795-2011.

Mishchenko, M. I., and L. D. Travis, 1998: Capabilities and limitations of a current FORTRAN implementation of the T-matrix method for randomly oriented, rotationally symmetric scatterers. *J. Quant. Spectrosc. Radiat. Transf.*, **60**, 309–324, doi:10.1016/S0022-4073(98)00008-9.

Mlawer, E. J., S. J. Taubman, P. D. Brown, M. J. Iacono, and S. A. Clough, 1997: Radiative transfer for inhomogeneous atmospheres: RRTM, a validated correlated-*k* model for the longwave. *J. Geophys. Res.*, **102**, 16 663–16 682, doi:10.1029/97JD00237.

Morrison, H., A. Morales, and C. Villanueva-Birriel, 2015: Concurrent sensitivities of an idealized deep convective storm to parameterization of microphysics, horizontal grid resolution, and environmental static stability. *Mon. Wea. Rev.*, **143**, 2082–2104, doi:10.1175/MWR-D-14-00271.1.

Palazzi, E., J. von Hardenberg, and A. Provenzale, 2013: Precipitation in the Hindu-Kush Karakoram Himalaya: Observations and future scenarios. *J. Geophys. Res. Atmos.*, **118**, 85–100, doi:10.1029/2012JD018697.

Parodi, A., and S. Tanelli, 2010: Influence of turbulence parameterizations on high-resolution numerical modeling of tropical convection observed during the TC4 field campaign. *J. Geophys. Res.*, **115**, D00J14, doi:10.1029/2009JD013302.

Prakash, S., A. K. Mitra, E. Rajagopal, and D. Pai, 2016: Assessment of TRMM-based TMPA-3B42 and GSMaP precipitation products over India for the peak southwest monsoon season. *Int. J. Climatol.*, **36**, 1614–1631, doi:10.1002/joc.4446.

Rasmussen, K. L., A. J. Hill, V. E. Toma, M. D. Zuluaga, P. J. Webster, and R. A. Houze, 2015: Multiscale analysis of three consecutive years of anomalous flooding in Pakistan. *Quart. J. Roy. Meteor. Soc.*, **141**, 1259–1276, doi:10.1002/qj.2433.

Sardar, S., I. Ahmad, S. S. Raza, and N. Irfan, 2012: Simulation of South Asian physical environment using various cumulus parameterization schemes of MM5. *Meteor. Appl.*, **19**, 140–151, doi:10.1002/met.266.

Skamarock, W. C., and Coauthors, 2008: A description of the Advanced Research WRF version 3. NCAR Tech. Note NCAR/TN-475+STR, 113 pp., doi:10.5065/D68S4MVH.

Stephens, G. L., and Coauthors, 2008: *CloudSat* mission: Performance and early science after the first year of operation. *J. Geophys. Res.*, **113**, D00A18, doi:10.1029/2008JD009982.

Tanelli, S., E. Im, S. L. Durden, L. Facheris, and D. Giuli, 2002: The effects of nonuniform beam filling on vertical rainfall velocity measurements with a spaceborne Doppler radar. *J. Atmos. Oceanic Technol.*, **19**, 1019–1034, doi:10.1175/1520-0426(2002)019<1019:TEONBF>2.0.CO;2.

——, S. L. Durden, E. Im, K. S. Pak, D. G. Reinke, P. Partain, J. M. Haynes, and R. T. Marchand, 2008: *CloudSat*'s cloud profiling radar after two years in orbit: Performance, calibration, and processing. *IEEE Trans. Geosci. Remote Sens.*, **46**, 3560–3573, doi:10.1109/TGRS.2008.2002030.

——, and Coauthors, 2011: NASA's Integrated Instrument Simulator Suite for Atmospheric Remote Sensing from Spaceborne Platforms (ISSARS) and its role for the ACE and GPM missions. *Earth Science Technology Forum*, Pasadena, CA, Jet Propulsion Laboratory, 5 pp. [Available online at https://esto.nasa.gov/2012test/conferences/estf2011/papers/Tanelli_ESTF2011.pdf.]

——, and Coauthors, 2012: Integrated instrument simulator suites for Earth Science. *Remote Sensing and Modeling of the Atmosphere, Oceans, and Interactions IV*, M. Kawamiya, T. N. Krishnamurti, and S. Maksyutov, Eds., International Society for Optical Engineering (SPIE Proceedings, Vol. 8529), 85290D, doi:10.1117/12.977577.

Thompson, G., P. R. Field, R. M. Rasmussen, and W. D. Hall, 2008: Explicit forecasts of winter precipitation using an improved bulk microphysics scheme. Part II: Implementation of a new snow parameterization. *Mon. Wea. Rev.*, **136**, 5095–5115, doi:10.1175/2008MWR2387.1.

Tian, Y., and C. D. Peters-Lidard, 2010: A global map of uncertainties in satellite-based precipitation measurements. *Geophys. Res. Lett.*, **37**, L24407, doi:10.1029/2010GL046008.

Ullah, K., and G. Shouting, 2013: A diagnostic study of convective environment leading to heavy rainfall during the summer monsoon 2010 over Pakistan. *Atmos. Res.*, **120–121**, 226–239, doi:10.1016/j.atmosres.2012.08.021.

Ushiyama, T., T. Sayama, Y. Tatebe, S. Fujioka, and K. Fukami, 2014: Numerical simulation of 2010 Pakistan flood in the Kabul River basin by using lagged ensemble rainfall forecasting. *J. Hydrometeor.*, **15**, 193–211, doi:10.1175/JHM-D-13-011.1.

Webster, P., V. Toma, and H.-M. Kim, 2011: Were the 2010 Pakistan floods predictable? *Geophys. Res. Lett.*, **38**, L04806, doi:10.1029/2010GL046346.

Winiger, M., M. Gumpert, and H. Yamout, 2005: Karakorum–Hindukush–western Himalaya: Assessing high-altitude water resources. *Hydrol. Processes*, **19**, 2329–2338, doi:10.1002/hyp.5887.

Yu, C., and M. Teixeira, 2014: Impact of non-hydrostatic effects and trapped lee waves on mountain-wave drag in directionally sheared flow. *Quart. J. Roy. Meteor. Soc.*, **141**, 1572–1585, doi:10.1002/qj.2459.

Yu, X., and T.-Y. Lee, 2010: Role of convective parameterization in simulations of a convection band at grey-zone resolutions. *Tellus*, **62A**, 617–632, doi:10.1111/j.1600-0870.2010.00470.x.